ASTROBIOLOGY Volume 22, Number 6, 2022 © Mary Ann Liebert, Inc. DOI: 10.1089/ast.2020.2396

> Open camera or QR reader and scan code to access this article and other resources online.



Freshwater and Evaporite Brine Compositions on Hadean Earth: Priming the Origins of Life

Nita Sahai. 1-3,i Segun Adebayo. 1 and Martin A. Schoonen 4,5

Abstract

The chemical composition of aqueous solutions during the Hadean era determined the availability of essential elements for prebiotic synthesis of the molecular building blocks of life. Here we conducted quantitative reaction path modeling of atmosphere-water-rock interactions over a range of environmental conditions to estimate freshwater and evaporite brine compositions. We then evaluated the solution chemistries for their potential to influence ribonucleotide synthesis and polymerization as well as protocell membrane stability. Specifically, solutions formed by komatiite and tonalite (primitive crustal rocks) weathering and evaporationrehydration (drying-wetting) cycles were studied assuming neutral atmospheric composition over a wide range of values of atmospheric partial pressure of CO₂ (P_{CO2}) and temperatures (T). Solution pH decreased and total dissolved concentrations of inorganic P, Mg, Ca, Fe, and C (P_T, Mg_T, Ca_T, Fe_T, and C_T) increased with increasing P_{CO2}. The P_{CO2} and T dictated how the solution evolved with regard to minerals precipitated and ions left in solution. At $T=75^{\circ}$ C and $P_{CO2}<0.05$ atm, the concentration ratio of magnesium to calcium ion concentrations (Mg^{2+}/Ca^{2+}) was < 1 and predominantly metal aluminosilicates (including clays), dolomite, gibbsite, and pyrite (FeS₂) precipitated, whereas at $P_{CO2} > 0.05$ atm, Mg^{2+}/Ca^{2+} was > 1 and mainly magnesite, dolomite, pyrite, chalcedony (SiO₂), and kaolinite (Al₂Si₂O₅) precipitated. At T=75°C and $P_{CO2} > 0.05$ atm, hydroxyapatite (HAP) precipitated during weathering but not during evaporation, and so, P_T increased with each evaporationrehydration cycle, while Mg_T, Ca_T, and Fe_T decreased as other minerals precipitated. At $T = 75^{\circ}$ C and $P_{CO2} \sim 5$ atm, reactions with komatite provided end-of-weathering solutions with high enough Mg²⁺ concentrations to promote RNA-template directed and montmorillonite-promoted nonenzymatic RNA polymerization, but incompatible with protocell membranes; however, montmorillonite-promoted RNA polymerization could proceed with little or no Mg^{2+} present. Cyclically evaporating/rehydrating brines from komatiite weathering at $T = 75^{\circ}C$ and $P_{CO2} \sim 5$ atm yielded the following: (1) high P_T values that could promote ribonucleotide synthesis, and (2) low divalent cation concentrations compatible with amino acid-promoted, montmorillonite-catalyzed RNA polymerization and with protocell membranes, but too low for template-directed nonenzymatic RNA polymerization. For all P_{CO2} values, Mg²⁺ and P_T concentrations decreased, whereas the HCO₃⁻ concentration increased within increasing temperature, due to the retrograde solubility of the minerals controlling these ions' concentrations; Fe²⁺ concentration increased because of prograde pyrite solubility. Tonalite weathering and cyclical wetting-drying reactions did not produce solution compositions favorable for promoting prebiotic RNA formation. Conversely, the ion concentrations compatible with protocell emergence, placed constraints on P_{CO2} of early Earth's atmosphere. In summary: (1) prebiotic RNA synthesis and membrane self-assembly could have been achieved even under neutral atmosphere conditions by atmosphere-water-komatiite rock interactions; and (2) constraints on element availability

School of Polymer Science and Polymer Engineering and ²Department of Geoscience, University of Akron, Akron, Ohio, USA.

³Integrated Bioscience Program, University of Akron, Akron, Ohio, USA.

⁴Environmental and Climate Sciences Department, Brookhaven National Laboratory, Upton, New York, USA. ⁵Department of Geosciences, Stony Brook University, Stony Brook, New York, USA.

ORCID ID (https://orcid.org/0000-0003-3852-0557).

for the origins of life and early $P_{\rm CO2}$ were addressed by a single, globally operating mechanism of atmosphere-water-rock interactions without invoking special microenvironments. The present results support a facile origins-of-life hypothesis even under a neutral atmosphere as long as other favorable geophysical and planetary conditions are also met. Key Words: Prebiotic chemistry—RNA—Protocell—Carbon dioxide—Weathering—Wetting-drying cycles—Komatiite. Astrobiology 22, 641–671.

1. Introduction

The prebiotic synthesis and self-assembly of the major molecular building blocks of life leading to the origins of life occurred in the presence of dissolved inorganic ions and minerals, but the ion concentration ranges present on early Earth have not been well-constrained to date. Nucleotides, adenosine phosphates, and membrane phospholipids all contain phosphate but the total dissolved inorganic phosphate concentration (P_T) is limited by the low solubility of hydroxyapatite $(HAP, Ca_{10}(PO_4)_6(OH)_2)$ observed on modern Earth, where P_T is at submillimolar levels. This is known as the "phosphate problem" (Gulick, 1955; Schwartz, 2006).

Model prebiotic experiments for nonenzymatic nucleotide synthesis, and nonenzymatic nucleotide polymerization, respectively, used much higher $P_T \sim 1~M$ (Powner et~al., 2009) and total dissolved magnesium concentration (Mg_T $\sim 80~\text{mM}$) (Ferris and Ertem, 1992; Adamala and Szostak, 2013) than biological, enzymatically catalyzed processes that occur at millimolar levels of these ions (Milo and Phillips, 2015). In comparison, montmorillonite-promoted activated ribonucleotide polymerization can proceed even in the total absence of magnesium, especially when cocatalysts, such as acidic α -amino acids or neutral, nonpolar α -amino acids, are present (Kaddour et~al., 2018; Namani et~al., 2021).

Ferrous iron has been proposed to have played the role of ${\rm Mg}^{2+}$ in prebiotic chemistry and early evolution of life. For example, ${\rm Fe}^{2+}$ (${\rm Fe}_{\rm T} \sim 80~{\rm mM}$) is more efficient than ${\rm Mg}^{2+}$ in catalyzing nonexymatic template-directed RNA polymerization (Jin *et al.*, 2018a) and ${\rm Fe}^{2+}$ can act as a cofactor in ribosomal RNA-catalyzed single-electron transfer reactions at much lower levels (µmolar) than ${\rm Mg}^{2+}$ (Hsiao *et al.*, 2013); furthermore, ${\rm Fe}^{2+}$ and other transition metals at millimolar concentrations can promote translation in bacteria (Bray *et al.*, 2018).

Another major building block of cells is the membrane, which is made up of phospholipids in extant life. Because of the complexity in synthesizing phospholipids, it is believed that protocell membranes were probably composed of simpler molecules called single-chain amphiphiles. Such molecules are found in meteorites and can be synthesized by Fischer-Tropsch synthesis pathways suggesting their prebiotic plausibility (Yuen and Kvenvolden, 1973; Deamer and Pashley, 1989; McCollom *et al.*, 1999; reviewed by Dalai *et al.*, 2016; Dalai and Sahai, 2019a, b).

The self-assembly of single-chain amphiphiles into model protocell membranes is sensitive to divalent cation concentrations above $\sim 1\text{--}2\,\text{mM}$. Thus, protocell membranes are disrupted at magnesium (Mg²+) and calcium (Ca²+) ion concentrations found in most modern environments and at the magnesium and ferrous ion concentrations (Fe²+) of $\sim 80\,\text{mM}$ used for RNA template-directed RNA polymerization (Brown and Silvius, 1989; Monnard and Deamer, 2002). In summary, nonenzymatic biomolecule synthesis and

protocell assembly at geochemically plausible ion concentrations are one of the grand challenges in understanding the origins of life (Dalai *et al.*, 2016; Sahai *et al.*, 2016).

Some recent studies have addressed the phosphate problem by using different approaches (e.g., Pasek, 2008; Pasek et al., 2013, 2014, 2017; Gull et al., 2015; Burcar et al., 2016, 2019; Karki et al., 2017; Gibard et al., 2017, 2019; Ritson et al., 2020; Huck et al., 2021), and we discuss them in detail below (Sections 4.2.1, 4.5.1, 4.5.2, 4.6). Furthermore, some of the incompatibilities between concentrations of divalent cations required for RNA template-directed RNA polymerization and protocell membrane stability have been resolved by recent reports. Specifically, two reports showed that mixed fatty acid-phospholipid membranes representing intermediate stages of protocell evolution are more stable in the presence of divalent cations than pure fatty acid membranes (Dalai et al., 2018; Jin et al., 2018b). Also, Mg²⁺-free RNA polymerization has been achieved by montmorillonite catalysis (Kaddour et al., 2018; Namani et al., 2021) and in coacervates (Poudyal et al., 2018, 2019). However, the problem may persist for the earliest fatty acidbased protocell membranes. The role of cations in peptide formation must also be considered. Wetting-drying cycles at $T \sim 65-85$ °C have been shown to promote peptide formation (Forsythe et al., 2015). In a natural geochemical environment, the concentrations of inorganic ions would also change with these cycles, and so, it would be important to know their effect on the peptide bond formation reaction.

Another important question is regarding the free uncomplexed ion concentrations versus the total dissolved concentration of the element. Modern intracellular concentration of total dissolved magnesium (Mg_T) varies from $\sim 30{-}100\,\mathrm{mM}$, although most of this magnesium is complexed to ligands leaving a free Mg²⁺ ion concentration of only $\sim 0.01{-}1\,\mathrm{mM}$ (Milo and Phillips, 2015). Modern intracellular concentration of total dissolved calcium (Ca_T) is $\sim 1{-}3\,\mathrm{mM}$ and free Ca²⁺ concentration is 10–100 nM (Milo and Phillips, 2015), while total dissolved iron levels (Fe_T) in blood range from $\sim 10{-}30\,\mu\mathrm{M}$. Total dissolved concentrations of ions are usually reported in prebiotic synthesis experiments rather than free, uncomplexed ion concentrations.

The goals of the present work were: (1) to constrain the concentrations ranges and speciation (free ion versus complexed ion concentrations) of phosphorus, magnesium, calcium and iron relevant to: (a) prebiotic RNA mononucletoide synthesis according to the experimental conditions used by Powner et al. (2009), (b) RNA polymerization by RNA template-mediation or by montmorillonite catalysis (e.g., Ferris and Ertem, 1992; Adamala and Szostak, 2013; Kaddour et al., 2018; Namani et al., 2021); and (c) protocell membrane self-assembly on Hadean Earth; and (2) to explore the suites of secondary minerals that could be stable under early Earth conditions because minerals can affect protocell membrane formation rates and stability (Hanczyc et al., 2003;

Sahai *et al.*, 2017), catalyze RNA and peptide polymerization (Ferris and Ertem, 1992; Kaddour *et al.*, 2018; Bedoin *et al.*, 2020; Namani *et al.*, 2021), and promote the generation of transmembrane pH gradients (Dalai and Sahai, 2020).

We used a well-established geochemical modeling approach called reaction path modeling to evaluate the chemical speciation of elements resulting from atmosphere-water-rock interactions, specifically, rock weathering and evaporation of the weathering-generated aqueous solution (Fig. 1), under a range of plausible early Earth environments of partial pressure of CO₂ (atmospheric P_{CO2}), temperature (T), and rock type. The importance of mineral-water interactions in the transition from geochemistry to biogeochemistry has been reviewed previously (Cleaves *et al.*, 2012; Belmonte and Mansy, 2016; Maurel and LeClerc, 2016; Sahai *et al.*, 2016; Schoonen and Smirnov, 2016) and, in the present study, we emphasize the critical role of atmosphere-water-rock interactions (Schoonen *et al.*, 2004; Tosca and McLennan, 2006; Schoonen and Smirnov, 2016; Hao *et al.*, 2017).

The geochemical reaction path modeling approach is based on mass balance, mass action and electroneutrality principles, and considers the distribution of elements between gases, solution and minerals. Reaction path modeling assuming partial equilbrium is widely used in geochemistry and environmental chemistry. This approach has even been applied to model the weathering mineralogy and potential aqueous solution chemistry of early Mars, and to estimate Hadean average river water and Europan ocean chemistry (McCollum, 1999; Schoonen *et al.*, 2004; Tosca and McLennan, 2006; Pasek and Greenberg, 2012; Schoonen and Smirnov, 2016; Hao *et al.*, 2017).

The first consideration for our study was the rock type available for weathering in the Hadean. The extent of oceanic versus continental crust in the first 500–700 Ma of Earth history is still hotly debated (Cawood *et al.*, 2012; Reimink *et al.*, 2014; Burnham and Berry, 2017; Rozel *et al.*, 2017). In any event, komatiite, an ultramafic-mafic, Mg-rich rock derived from primitive mantle peridotite, is almost exclusively of Hadean (~4.45–4.2 Ga) and Archean (~4.2–2.5 Ga) age. This rock comprised the earliest submarine oceanic crust as well as subaerial oceanic islands (Prothero and Dott, 2002, p 119) (Fig. 2).

The Acasta Gneiss (~ 3.9 –4.03 Ga), the oldest rock known, is a metamorphosed tonalite/granodiorite representing ancient continental crust (Iizuka *et al.*, 1996) (Fig. 2). Supporting the idea of very ancient protocontinental crust, stabilization of liquid water at temperatures of ~ 75 –80°C and protocontinent formation as early as ~ 4.2 Ga is suggested by radiometric dating of detrital zircons (Peck *et al.*, 2001). However, temperatures may also have been cooler since the luminosity of the young Sun was lower ("faint young Sun").

Subaerial weathering of the komatiite or tonalite rocks would occur in equilibrium with atmospheric gases, thus releasing ions into solution, followed by a hydrologic cycle including evaporation (Fig. 1). The weathering and evaporation reactions produce secondary (sedimentary) minerals. The chemical composition of major, minor and accessory phase minerals in komatiite and tonalite, and subsequent precipitation of secondary minerals determine the postweathering solution compositions along with the chemistry of the atmosphere (Table 1 and Fig. 2).

Based on atmospheric composition and chemical composition of the minerals in komatiite and tonalite, 14 elements were included. The distribution of these 14 elements among all the gases, minerals and aqueous species of the thermodynamic database (Thermo) of the modeling software, The Geochemist's Workbench (GWB) (Bethke, 2008), was considered over a wide range of $P_{\rm CO2}$ values (present atmospheric level (PAL) to 30 atm) and temperatures (75–25°C) to account for the faint young Sun.

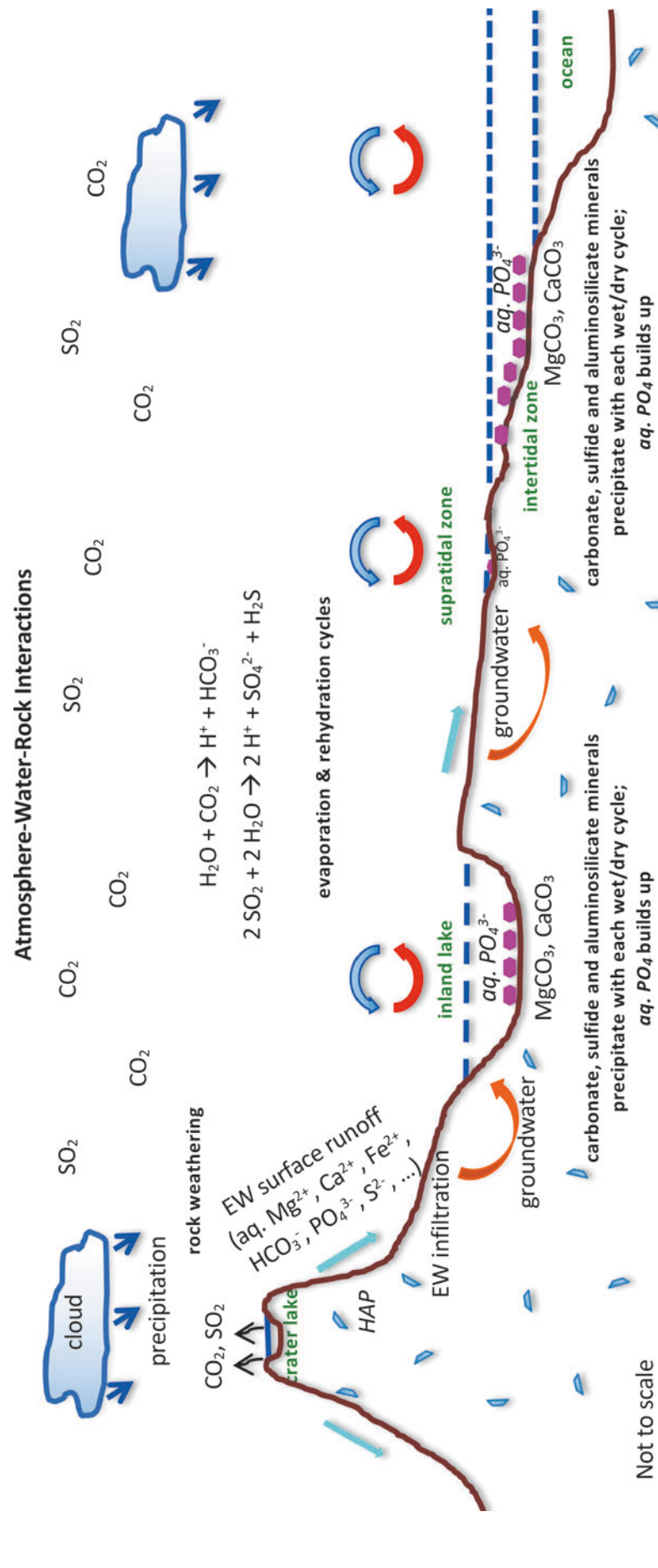
For our purposes, we considered dissolved phosphate, magnesium, and calcium concentrations on the order of magnitude of millimolal as the "biological level" and 10s of micromolar as the biological level for iron. The concentrations of phosphorus, magnesium, calcium, and iron consistent with prebiotic RNA monomer synthesis (Powner et al., 2009), RNA polymerization (Ferris and Ertem, 1992; Adamala and Szostak, 2013; Kaddour et al., 2018; Namani et al., 2021), and protocell membrane stability on Hadean Earth (Monnard and Deamer, 2002; Dalai et al., 2018) have already been discussed above. Finally, we discuss the implications of our results and the effect of atmospheric redox states for prebiotic chemistry. The most significant outcome of the present study is that prebiotic synthesis could potentially have occurred even under neutral atmospheric conditions within the framework of a single unified mechanism of average, global atmosphere-water-komatiite rock interactions. This is achieved without requiring special microenvironments, although special environments would certainly have existed and could have contributed to the total inventory of organics and to the emergence of the earliest protocells.

2. Methods

The reaction path geochemical modeling approach taken here is based on mass balance, mass action, and electroneutrality principles. Calculations were performed by using the GWB software package (Bethke, 2008) with the thermodynamic database called Thermo, which was originally compiled for the geochemical modeling program EQ3/EQ6 (Wolery, 1992a, 1992b) from the Lawrence Livermore National Laboratory.

We used the Thermo database because its solubility product for HAP is accurate, whereas HAP solubility products provided in the other databases of GWB are inaccurate (Sahai and Schoonen, 2020). The Thermo database contains reaction stoichiometries and equilibrium constants, as well as enthalpies and entropies for reactions involving 10 gases, 624 minerals, and 551 aqueous species. The major and minor elements present in komatiite and tonalite, and the major atmospheric gases present yield the 14 important elements considered here, namely, Al, C, Ca, Cl, Fe, H, K, Mg, N, Na, O, P, S and Si.

The slow reaction kinetics of water-aluminosilicate rock interactions at low temperatures is accounted for in two ways. First, in the weathering step, the reaction is allowed to proceed to only partial equilibrium. In the subsequent evaporation step, secondary minerals that are known to be kinetically slow to precipitate are suppressed (prevented from precipitating) in the model calculations. Note that in geochemical terminology, the term "primary minerals" denotes minerals that are those produced by cooling of molten magma or lava; "secondary minerals" denotes those



freshwater, groundwater and evaporative lakes and brines. Thermodynamic equilibria between atmospheric gases, aqueous solutions and solid phases control the dissolution of In detail, volcanoes release atmospheric gases, such as CO2 and SO2, which dissolve into rainwater, which makes the rainwater acidic. Dissolved SO2 disproportionates into solutions occurs in evaporative basins and form brines with new chemical compositions after each wetting-drying cycle. After evaporation, the resulting solution is called "End of Evaporation (EE)" solution in the present study. Turquoise blue and ochre arrows indicate directions of surface runoff and groundwater flow, respectively; red and blue Schematic representing the global process of atmosphere-water-rock interactions, that control element concentrations in environmental niches, such as surface SO₄²⁻ and H₂S gas. Subaerial weathering of surface rocks by this acidic rainwater releases ions into surface runoff. This solution is called "End of Weathering (EW)" solution in the present study. This solution also infiltrates into the ground and causes subsurface weathering (not considered in the present study). Evaporation and rehydration of the surface minerals in the rocks, precipitation of secondary minerals and the simultaneous evolution of the solution compositions during rock weathering and solution evaporation reactions. arrows indicate cyclical wetting-drying events on land and over the ocean. Figure is not drawn to scale. HAP, hydroxyapatite. Drawing inspired by Damer and Deamer (2015).

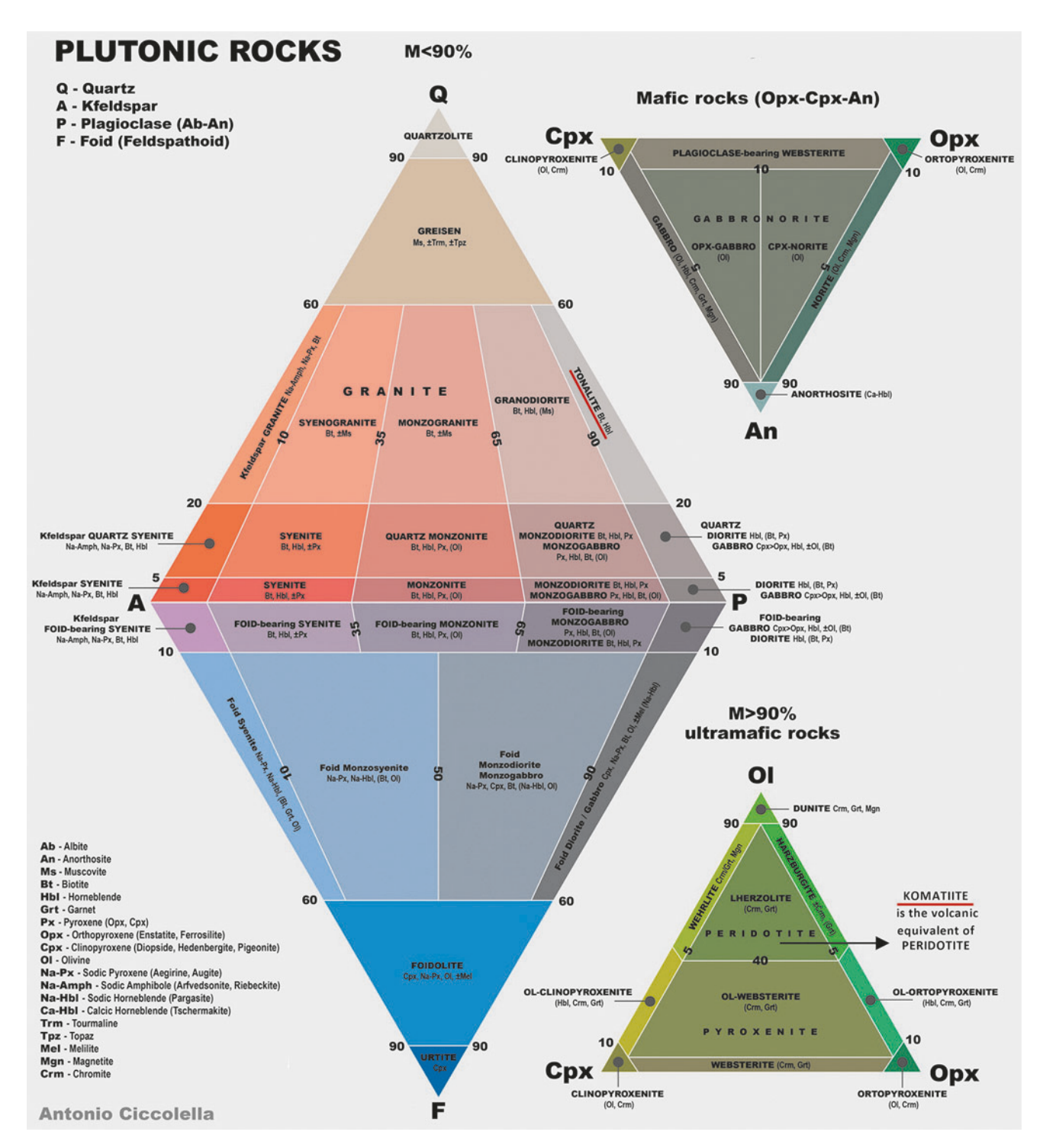


FIG. 2. IUGS classification of plutonic (intrusive) igneous rocks based on their mineralogical and chemical compositions. Komatiite is the volcanic (extrusive) equivalent of peridotite. Komatiite and tonalite are highlighted by red underline. IUGS, International Union of Geological Sciences; Q, Quartz; A, Alkali feldspars; P, Plagioclase; F, Feldspathoids; An, Anorthite; Cpx, clinopyroxene; Opx, orthopyroxene; Ol, olivine. Modified from https://en.wikipedia.org/wiki/QAPF_diagram.

that are formed by weathering reactions (and does not imply relatively lower importance); and "accesory phase" refers to those minerals that are present in only minor quantities.

In detail, we allowed the weathering of either komatiite or tonalite to proceed to only partial (5%) equilibrium. The resulting solution is named "end-of-weathering (EW)" solution.

In essence, the evaporation is equivalent to the removal of 950 g out of 1 kg of the solvent, water. The wetting-drying cycling is induced by taking the final EE brine, containing 50 g of water, and adding 950 g of EW solution to simulate rehydration. This wetting-drying process was repeated for up to 10 cycles. Also, minerals that are known to precipitate slowly at low temperatures are suppressed in

TABLE 1. KOMATIITE AND TONALITE MINERALOGICAL COMPOSITIONS USED TO MODEL WEATHERING REACTIONS

| Mineral | Komatiite | Tonalite |
|--|-----------|----------|
| Enstatite (MgSiO ₃) | 65 | 0 |
| Forsterite (Mg ₂ SiO ₄) | 500 | 0 |
| Diopside (MgCaSi ₂ O ₆) | 170 | 0 |
| Ferrosilite (FeSiO ₃) | 45 | 0 |
| Anorthite (CaAl ₂ Si ₂ O ₈) | 165 | 250 |
| Albite (NaAlSi ₃ O ₈) | 55 | 250 |
| Pargasite (NaCa ₂ Al ₃ Mg ₄ Si ₆ O ₂₂ (OH) ₂) | 0 | 150 |
| Annite (KFe ₃ AlSi ₃ O ₁₀ (OH) ₂) | 0 | 100 |
| Phlogopite (KAlMg ₃ SiO ₁₀ (OH) ₂) | 0 | 50 |
| Quartz (SiO ₂) | 0 | 200 |
| Hydroxyapatite (Ca ₁₀ (PO ₄) ₆ (OH) ₂) | 1, 10 | 1, 10 |

| Secondary mineral | Chemical formula |
|-------------------|---|
| Saponite-Mg | Mg _{3.165} Al _{0.33} Si _{3.67} O ₁₀ (OH) ₂ |
| Saponite-Ca | $Ca_{0.165}Mg_3Al_{0.33}Si_{3.67}O_{10}(OH)_2$ |
| Saponite-Na | $Na_{0.33}Mg_3Al_{0.33}Si_{3.67}O_{10}(OH)_2$ |
| Amesite | $Mg_4Al_4Si_2O_{10}(OH)_8$ |
| Gibbsite | $Al(OH)_3$ |
| Kaolinite | $Al_2Si_2O_5(OH)_4$ |
| Chalcedony | SiO_2 |
| Dolomite | $(Ca,Mg)(CO_3)_2$ |
| Magnesite | $MgCO_3$ |
| Hydromagnesite | $Mg_5(CO_3)_4(OH)_2.4H_2O$ |
| Calcite | CaCO ₃ |
| Pyrite | FeS_2 |
| Analcime | NaAlSi ₂ O ₆ .H ₂ O |
| Dawsonite | $NaAl(CO_3)(OH)_2$ |
| Huntite | $CaMg_3(CO_3)_4$ |
| Clinoptilolite-Ca | $CaAl_2Si_{10}O_{24}.8H_2O$ |
| Clinoptilolite-Na | $Na_2Al_2Si_{10}O_{24}.8H_2O$ |
| Muscovite | KAl ₃ Si ₃ O ₁₀ (OH) ₂ |
| | |

Compositions are in g/kg of rock. Modified from Schoonen *et al.* (2004). Also shown are the secondary minerals formed by weathering of the primary rocks, komatiite and tonalite, and by evaporation of the resulting end-of-weathering solutions.

HAP=hydroxyapatite.

these calculations. During the wetting-drying cycles, the entire mass of precipitated minerals is allowed to remain in contact with the solution.

The mineralogy of a rock determines its major, minor and trace element concentrations. The average mole percentage of major rock-forming minerals is well-established, but concentrations of trace elements are more variable. Weathering of the various minerals in the rock releases magnesium, calcium, iron, alkali cations, phosphate and silica. The major rock-forming minerals, which are often solid solutions between well-defined end-members, are represented as mixtures of pure end-member minerals (Table 1). The major primary minerals in komatiites are the Mg-enriched minerals, forsterite (Mg₂SiO₄) and enstatite (MgSiO₃), and the Ca-rich plagioclase, anorthite (CaAl₂Si₂O₈); other minor mineral phases may also be present. Ferrosilite (FeSiO₃), which is present in very small amounts in komatiite, and annite (KFe₃AlSi₃O10(OH)₂) in tonalite, respectively, are the sources of iron.

In tonalite, the major primary minerals are quartz, anorthite, albite, pargasite, phlogopite, and annite; other minor mineral phases such as HAP may also be present (Table 1).

Primary HAP is the phosphate source in both rocks. We modeled rocks with primary HAP contents ($c_{HAP, p}$) of 1 and 10 g HAP per kg of rock (Mielke, 1979) and reacted the rock with 1 kg of water.

Equilibrium with atmospheric CO_2 gas determines the total dissolved inorganic carbonate concentration (C_T). Estimates for Hadean and Archean P_{CO2} span a huge range of six orders of magnitude from 10^{-4} atm up to 100 atm before carbonate mineral recycling into the Earth's mantle began (Walker, 1985; Kasting, 1993; Siegfried *et al.*, 2002; Zahnle, 2006; Zahnle *et al.*, 2010; Jackson and Jellinek, 2015; Catling and Kasting, 2017; Sossi *et al.*, 2020). We chose P_{CO2} values of P_{CO2} values of P_{CO2} atm, P_{CO2} atm, P_{CO2} atm to explore the influence of P_{CO2} on solution compositions. Beyond 30 atm, the pressure dependence of equilibria is not well-constrained and P_{CO2} may exist as a separate liquid phase.

The redox equilibria were set as follows. We assumed that CO₂ did not undergo redox reactions, reflecting the high-energy barrier for abiotic CO₂ reduction at Earth's surface conditions. For sulfur species, the conditions were set as follows. Sulfur dioxide (SO₂) is expected to be part of volcanic emissions and would essentially fully dissolve in water, resulting in the formation of both H₂S and SO_4^{2-} by disproportionation reactions (Johnston, 2011) (Fig. 1). We set atmospheric $P_{H2S} = 1 \times 10^{-6}$ atm (Holland, 1984; Rickard, 2012) and a dissolved sulfate concentration of 200 µM (Holland, 2004) to buffer sulfide redox chemistry. We also conducted a sensitivity analysis of the effects of varying PH2S over eight orders of magnitude and SO_4^{2-} concentrations over 4 orders of magnitude on P_T, Mg_T and Ca_T and Fe_T. Finally, the oxidation of Fe(II) to Fe(III) is not considered here. Phosphorous is considered only in its pentavalent state. HAP and whitlockite are the calcium phosphate minerals included in the Thermo database.

Oxygen (18 O) isotope values measured in the oldest age zircon (\sim 4.2 Ga) indicate that the crystal grew in equilibrium with solutions at $T \sim 75^{\circ}$ C (Peck *et al.*, 2001). To account for the lower solar luminosity on early Earth, which could result in lower temperatures, we also modeled a subset of reactions in the temperature range of 25–75°C.

Specific minerals that are kinetically slow to precipitate at low temperatures were suppressed, namely: akermanite, albite, andradite, antigorite, chrysotile, clinochlore, dicalcium silicate, diopside, foshagite, greenalite, grossular, hedenbergite, hillebrandite, magnesite (at 25°C only), merwinite, minnesotaite, monticellite, ordered dolomite (at 25°C only), phlogopite, pseudowollastonite, quartz, rankinite, ripidolite, tridymite, tremolite, wollastonite, and tobermorite. The concentration of dissolved silica was set by the solubility of chalcedony.

Note that the *total* dissolved element concentration for element X (X_T) (*e.g.*, magnesium, calcium, iron, phosphate, and carbon) includes the concentrations of the free uncomplexed cation or anion (Xⁿ⁺ or Xⁿ⁻), as well as all inorganic cation-ligand complexes. GWB program uses free magnesium ion (Mg²⁺), free calcium ion (Ca²⁺), free ferrous ion (Fe²⁺), HPO₄²⁻, and HCO₃⁻ as the "basis species" for the corresponding elements, and also provides an equilibrium calculation of the speciation of these basis species. We

report P_T , Mg_T , Mg^{2+} , Ca_T and Ca^{2+} ; total dissolved concentration of carbon (C_T) ; and Fe_T , which is almost entirely present as Fe^{2+} .

Finally, we note that complexation of inorganic ions to organic species as well as surface complexation on minerals would change the speciation and free ion concentrations. The complexation of ions with organics will be addressed in a subsequent study. We did not account for surface complexation in the present work because the GWB software includes only the surface complexation constant for ferrihydrite consistent with the Double Layer Model (Dzombak and Morel, 1990) and hydrous ferric oxide or other iron oxyhydroxides are not expected to have been thermodynamically stable or kinetically long-lived under Hadean Earth conditions.

3. Results

3.1. Subaerial weathering of komatiite and subsequent evaporation

3.1.1. Weathering. All solutions reacted with komatiite containing 1 g HAP/kg of komatiite were in equilibrium with atmospheric composition defined by various values of P_{CO2} and constant value of P_{H2S} (see Section 2 Methods). At 75°C, the solutions at the start of the weathering reaction path (reaction progress variable $\xi = 0$) had acidic pHs at all P_{CO2} values considered, which evolved toward more neutral values during the weathering reaction and even reached basic values for some systems by the end of the reaction path (reaction progress variable $\xi = 1$) (Fig. 3 and Table 2). EW solution compositions from komatiite showed that the final pH decreased consistently from alkaline (\sim 9) at PAL to acidic (5.7 and lower) at $P_{CO2} \ge 5$ atm (Fig. 3 and Table 2). Total dissolved element concentrations of phosphorus, magnesium, calcium, iron, and carbon increased with increasing P_{CO2} (Fig. 3 and Table 2).

The higher concentrations of dissolved elements are consistent with the greater solubility of aluminosilicate and carbonate minerals at lower pH. Solution ionic strength increased by one order of magnitude from millimolal to 10s of millimolal with increasing $P_{\rm CO2}$ from PAL to 20 atm. Increasing the HAP content of the komatiite to 10 g HAP/kg of rock did not affect the solution composition (Fig. 3). Biologically relevant concentrations for each element are indicated by the green lines in Fig. 3. The millimolal level is achieved for Mg_T at $P_{\rm CO2}$ =1 atm, while Fe_T is micromolar at this $P_{\rm CO2}$; however, the concentrations of $P_{\rm T}$ and $Ca_{\rm T}$ remain at $\sim 1 \times 10^{-4}$ molal even up to $P_{\rm CO2}$ =30 atm, and a high $C_{\rm T} \ge 1 \times 10^{-2}$ molal is obtained for all values of $P_{\rm CO2} \ge 0.05$ atm.

The komatiite weathering reaction path is shown in terms of the secondary minerals precipitated and evolution of the solution composition at selected values of P_{CO2} (Fig. 4); mineral chemical compositions are reported in Table 1. The reaction progress variable (ξ) is plotted on the x axis from 0 to 1. It can be seen that the suite of minerals precipitated up to $P_{CO2} = 10 \times PAL$ is similar, whereas the minerals precipitated at $P_{CO2} \ge 0.5$ atm are different. Also, the final solution Ca^{2+}/Mg^{2+} is >1 up to $P_{CO2} = 10 \times PAL$ and Ca^{2+}/Mg^{2+} is <<1 at $P_{CO2} \ge 0.5$ atm. In detail, up to $P_{CO2} = 10 \times PAL$, metal aluminosilicates (predominantly, clay minerals Mgsaponite, Na-saponite, Ca-saponite, smectite and amesite),

carbonate (ordered dolomite; note that dolomite precipitation is not inhibited at temperatures greater than $\sim 60^{\circ}$ C; Hardie, 1987; Romanek *et al.*, 2009), aluminum hydroxide (gibbsite), pyrite, and HAP are formed.

At higher values of P_{CO2} , carbonates (magnesite and ordered dolomite) predominate; saponite is no longer formed; pyrite and HAP are still formed, but metal aluminosilicates are replaced by silica (chalcedony) and pure aluminosilicate (kaolinite). The precipitation of saponites (Mg-enriched clay) at lower values of P_{CO2} but not at higher values is important in controlling Mg^{2+} concentration in solution, along with the precipitation of magnesite and dolomite. These differences in solution behavior and secondary minerals formed at low versus high values of P_{CO2} will be discussed below in terms of the concept of the "geochemical divide." Indeed, as we will see below, these differences are already evident at $P_{CO2} \ge 0.005$ atm.

3.1.2. Evaporation. EW solutions infiltrate to form groundwater, run off the surface or collect in local topographic depressions forming inland and crater lakes, ultimately, reaching the littoral zone (Fig. 1). The EW composition at each P_{CO2} provided the starting solution for evaporation at 75°C. From the start of the evaporation reaction path ($\xi = 0$) to the end ($\xi = 1$), solution pH does not change much (maximum change of ~ 0.9 pH units), which can be seen by comparing the final EW pH in Table 2 Section A with final the EE pH in Table 2 Section B at any particular P_{CO2} value (Fig. 3 and Table 2). As with EW solutions, the final pH decreases, whereas the total dissolved concentrations of phosphorus, magnesium, calcium, iron, and carbon increase with increasing P_{CO2} . Again, the greater solubility is consistent with the more acidic pH values at higher P_{CO2} values.

At each P_{CO2} , evaporation results in a decrease in the concentrations of Mg_T , Ca_T , and Fe_T but P_T and C_T increase compared with their concentrations in the EW solutions (Fig. 3 and Table 2). Millimolal levels of Mg_T are obtained at $P_{CO2} = 20$ atm. By $P_{CO2} = 5$ atm, millimolal P_T and micromolar Fe_T are observed; concentrations of Ca_T are micromolal to submicromolal at almost all P_{CO2} values. Solution ionic strength does not change significantly (remains in the same order of magnitude) with P_{CO2} . Increasing the HAP content of the komatiite to $10 \, g$ HAP/kg of rock does not affect the solution composition (Fig. 3).

The evaporation reaction path is shown in terms of the secondary minerals precipitated and evolution of solution composition at selected values of $P_{\rm CO2}$ (Fig. 5); mineral chemical compositions are reported in Table 1. As with the weathering system, there is a difference in the suite of minerals precipitated and reversal in the ${\rm Ca^{2+}/Mg^{2+}}$ ratio at $P_{\rm CO2}$ values < 0.5 atm compared with $P_{\rm CO2}$ values > 0.5 atm.

The discussion below on the geochemical divide shows that these differences are already evident at $P_{\rm CO2} \! \ge \! 0.005$ atm. In particular, at lower values of $P_{\rm CO2}$, the predominant minerals for the evaporation reaction path are Na-Al silicates (analcime) and various carbonates (dawsonite, calcite, and ordered dolomite), whereas the minerals precipitated at higher $P_{\rm CO2}$ values are mainly carbonates (magnesite, ordered dolomite, and dawsonite) and silica (chalcedony) (Fig. 5). Pyrite is formed at all values of $P_{\rm CO2}$, but HAP is not precipitated at any $P_{\rm CO2}$ (Fig. 5).

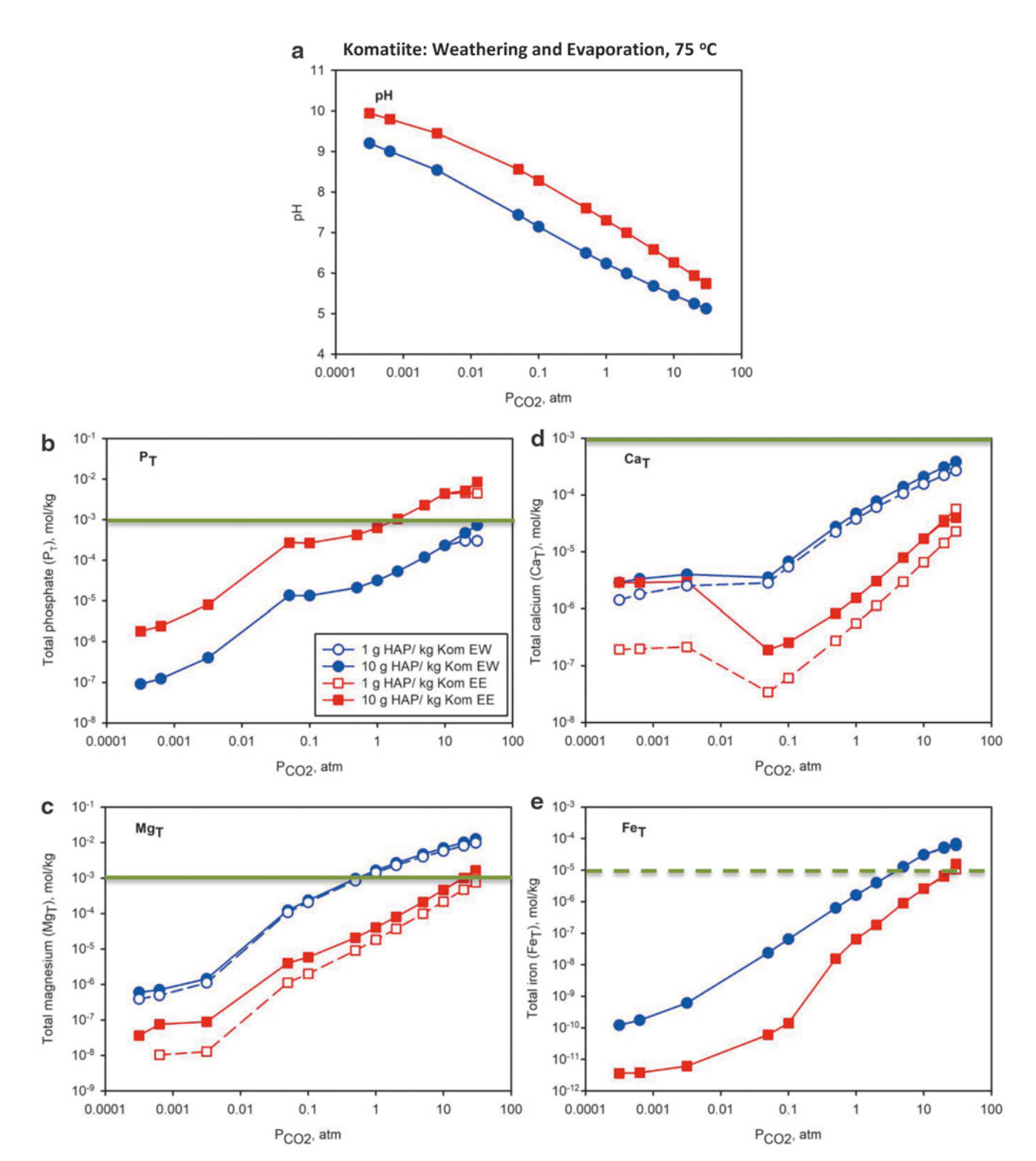


FIG. 3. Komatiite (kom) EW (blue symbols) and EE (red symbols) solution chemistry at 75° C as a function of various values of P_{CO2} for komatiite containing with low and high primary HAP content ($c_{HAP, p}$) (empty and filled symbols, respectively). (a) pH and concentrations (molal) of (b) total phosphate (P_{T}), (c) total magnesium (Mg_{T}), (d) total calcium (Ca_{T}), and (e) total iron (Fe_{T} = $Fe(II)_{T}$). Solid green lines indicate biologically relevant concentrations of P_{T} , Mg_{T} , Ca_{T} and dashed green line indicates biologically relevant concentration of Fe_{T} . Compare with Fig. 14 for tonalite weathering at 75° C. EW, end-of-weathering; EE, end-of-evaporation; P_{CO2} , partial pressure of CO_2 .

| Table 2. | KOMATIITE WEATHERI | ING AND EVAPORATIO | ON SOLUTION CHEMISTRY | | | | |
|--|--------------------|--------------------|-----------------------|--|--|--|--|
| AT 75°C AND VARIOUS PARTIAL PRESSURES OF CO ₂ | | | | | | | |

| 11 | 7 C | D | М- | 14-2+ | | <i>C</i> | C-2+ | |
|---|--|----------------------------------|----------------------------------|----------------------------------|----------------------------------|---|----------------------------------|---|
| рн | 1.5. | P_T | Mg_T | Mg ⁻ | Fe_T | Ca_T | Ca | C_T |
| (A) EW concentrations \log_{10} (molal) | | | | | | | | |
| 9.1 | -2.21 | -7.04 | -6.22 | -6.41 | -9.91 | -5.54 | -5.85 | -2.39 |
| 9 | -2.17 | | -6.15 | -6.31 | -9.76 | -5.48 | -5.75 | -2.30 |
| 8.5 | -2.01 | -6.39 | -5.84 | -5.95 | -9.21 | -5.40 | -5.60 | -2.08 |
| 7.4 | -1.95 | -4.87 | -3.91 | -3.97 | -7.62 | -5.45 | -5.55 | -1.96 |
| 7.1 | -1.94 | -4.87 | -3.63 | -3.69 | -7.19 | -5.17 | -5.27 | -1.92 |
| 6.5 | -1.87 | -4.68 | -3.02 | -3.08 | -6.20 | -4.56 | -4.65 | -1.72 |
| 6.2 | -1.82 | -4.50 | -2.79 | -2.85 | -5.79 | -4.33 | -4.42 | -1.56 |
| 6 | -1.74 | -4.27 | -2.58 | -2.64 | -5.40 | -4.11 | -4.22 | -1.35 |
| 5.7 | -1.63 | -3.93 | -2.33 | -2.40 | -4.90 | -3.86 | -3.97 | -1.03 |
| 5.4 | -1.53 | -3.63 | -2.16 | -2.24 | -4.51 | -3.68 | -3.81 | -0.77 |
| 5.2 | -1.42 | -3.52 | -2.00 | -2.09 | -4.30 | -3.51 | -3.66 | -0.49 |
| 5.1 | -1.36 | -3.52 | -1.91 | -2.01 | -4.22 | -3.42 | -3.57 | -0.33 |
| ations log | (molal) | | | | | | | |
| 9.9 | -0.84 | -5.74 | -7.44 | n.d. | -11.44 | -5.54 | -6.71 | -1.22 |
| 9.7 | -0.80 | -5.61 | -7.12 | -7.99 | -11.42 | -5.54 | -6.70 | -1.13 |
| 9.4 | -0.66 | -5.09 | -7.05 | -7.90 | -11.21 | -5.53 | -6.67 | -0.89 |
| 8.5 | -0.67 | -3.57 | -5.40 | -5.95 | -10.22 | -6.72 | -7.47 | -0.73 |
| 8.2 | -0.68 | -3.57 | -5.23 | -5.70 | -9.85 | -6.59 | -7.22 | -0.71 |
| 7.6 | -0.69 | -3.38 | -4.68 | -5.04 | -7.80 | -6.08 | -6.56 | -0.69 |
| 7.3 | -0.69 | -3.20 | -4.40 | -4.74 | -7.19 | -5.81 | -6.26 | -0.68 |
| 6.9 | -0.70 | -2.98 | -4.10 | -4.43 | -6.74 | -5.52 | -5.95 | -0.66 |
| 6.5 | -0.71 | -2.64 | -3.68 | -4.01 | -6.04 | -5.10 | -5.52 | -0.59 |
| 6.2 | -0.72 | -2.36 | -3.33 | -3.67 | -5.59 | -4.77 | -5.18 | -0.49 |
| 5.9 | -0.73 | -2.34 | -3.00 | -3.33 | -5.20 | -4.44 | -4.85 | -0.34 |
| 5.7 | -0.75 | -2.35 | -2.80 | -3.12 | -4.97 | -4.24 | -4.64 | -0.22 |
| | 9.1 9 8.5 7.4 7.1 6.5 6.2 6 5.7 5.4 5.2 5.1 ations log 9.9 9.7 9.4 8.5 8.2 7.6 7.3 6.9 6.5 6.2 5.7 5.4 5.2 5.1 | rations \log_{10} (molal) 9.1 -2.21 -7.04 -6.22 -6.41 -9.91 9 -2.17 -6.91 -6.15 -6.31 -9.76 8.5 -2.01 -6.39 -5.84 -5.95 -9.21 7.4 -1.95 -4.87 -3.91 -3.97 -7.62 7.1 -1.94 -4.87 -3.63 -3.69 -7.19 6.5 -1.87 -4.68 -3.02 -3.08 -6.20 6.2 -1.82 -4.50 -2.79 -2.85 -5.79 6 -1.74 -4.27 -2.58 -2.64 -5.40 5.7 -1.63 -3.93 -2.33 -2.40 -4.90 5.4 -1.53 -3.63 -2.16 -2.24 -4.51 5.2 -1.42 -3.52 -2.00 -2.09 -4.30 5.1 -1.36 -3.52 -1.91 -2.01 -4.22 rations \log_{10} (molal) 9.9 -0.84 -5.74 -7.44 n.d11.44 9.7 -0.80 -5.61 -7.12 -7.99 -11.42 9.4 -0.66 -5.09 -7.05 -7.90 -11.21 8.5 -0.67 -3.57 -5.40 -5.95 -10.22 8.2 -0.68 -3.57 -5.23 -5.70 -9.85 7.6 -0.69 -3.38 -4.68 -5.04 -7.80 7.3 -0.69 -3.20 -4.40 -4.74 -7.19 6.9 -0.70 -2.98 -4.10 -4.43 -6.74 6.5 -0.71 -2.64 -3.68 -4.01 -6.04 6.2 -0.72 -2.36 -3.33 -3.67 -5.59 5.9 -0.73 -2.34 -3.00 -3.33 -5.20 | rations \log_{10} (molal) 9.1 | rations \log_{10} (molal) $9.1 - 2.21 - 7.04 - 6.22 - 6.41 - 9.91 - 5.54 - 5.85 9 - 2.17 - 6.91 - 6.15 - 6.31 - 9.76 - 5.48 - 5.75 8.5 - 2.01 - 6.39 - 5.84 - 5.95 - 9.21 - 5.40 - 5.60 7.4 - 1.95 - 4.87 - 3.91 - 3.97 - 7.62 - 5.45 - 5.55 7.1 - 1.94 - 4.87 - 3.63 - 3.69 - 7.19 - 5.17 - 5.27 6.5 - 1.87 - 4.68 - 3.02 - 3.08 - 6.20 - 4.56 - 4.65 6.2 - 1.82 - 4.50 - 2.79 - 2.85 - 5.79 - 4.33 - 4.42 6 - 1.74 - 4.27 - 2.58 - 2.64 - 5.40 - 4.11 - 4.22 5.7 - 1.63 - 3.93 - 2.33 - 2.40 - 4.90 - 3.86 - 3.97 5.4 - 1.53 - 3.63 - 2.16 - 2.24 - 4.51 - 3.68 - 3.81 5.2 - 1.42 - 3.52 - 2.00 - 2.09 - 4.30 - 3.51 - 3.66 5.1 - 1.36 - 3.52 - 1.91 - 2.01 - 4.22 - 3.42 - 3.57 ations \log_{10} (molal) 9.9 - 0.84 - 5.74 - 7.44 n.d 11.44 - 5.54 - 6.71 9.7 - 0.80 - 5.61 - 7.12 - 7.99 - 11.42 - 5.53 - 6.67 9.4 - 0.66 - 5.09 - 7.05 - 7.90 - 11.21 - 5.53 - 6.67 8.5 - 0.67 - 3.57 - 5.40 - 5.95 - 10.22 - 6.72 - 7.47 8.2 - 0.68 - 3.57 - 5.23 - 5.70 - 9.85 - 6.59 - 7.22 7.6 - 0.69 - 3.38 - 4.68 - 5.04 - 7.80 - 6.08 - 6.56 7.3 - 0.69 - 3.20 - 4.40 - 4.74 - 7.19 - 5.81 - 6.26 6.9 - 0.70 - 2.98 - 4.10 - 4.43 - 6.74 - 5.52 - 5.95 6.5 - 0.71 - 2.64 - 3.68 - 3.33 - 3.67 - 5.59 - 4.77 - 5.18 5.9 - 0.73 - 2.34 - 3.00 - 3.33 - 5.20 - 4.44 - 4.85 9.0 - 0.70 - 2.98 - 4.10 - 4.43 - 6.74 - 5.52 - 5.95 6.5 - 0.73 - 2.34 - 3.00 - 3.33 - 5.20 - 4.44 - 4.85 9.0 - 0.70 - 2.98 - 4.10 - 4.43 - 6.74 - 5.52 - 5.95 6.5 - 0.71 - 2.64 - 3.68 - 3.37 - 5.50 - 3.33 - 5.20 - 4.44 - 4.85 9.0 - 0.73 - 2.34 - 3.00 - 3.33 - 5.20 - 4.44 - 4.85 9.0 - 0.73 - 2.34 - 3.00 - 3.33 - 5.20 - 4.44 - 4.85 9.0 - 0.73 - 2.34 - 3.00 - 3.33 - 5.20 - 4.44 - 4.85 9.0 - 0.73 - 2.34 - 3.00 - 3.33 - 5.20 - 4.44 - 4.85 9.0 - 0.73 - 2.34 - 3.00 - 3.33 - 5.20 - 4.44 - 4.85 9.0 - 0.73 - 2.34 - 3.00 - 3.33 - 5.20 - 4.44 - 4.85 9.0 - 0.73 - 2.34 - 3.00 - 3.33 - 5.20 - 4.44 - 4.85 9.0 - 0.73 - 2.34 - 3.00 - 3.33 - 5.20 - 4.44 - 4.85 9.0 - 0.73 - 2.34 - 3.00 - 3.33 - 5.20 - 4.44 - 4.85 9.0 - 0.73 - 2.34 - 3.00 - 3.33 - 5.20 - 4.44 - 4$ |

Solution pH and concentrations of total phosphate (P_T) , total magnesium (Mg_T) , free magnesium ion (Mg^{2+}) , total iron (Fe_T) , total calcium (Ca_T) , free calcium ion (Ca^{2+}) , and total carbonate (C_T) after 5% weathering of komatiite (A) and after subjecting the EW solution to one cycle of 95% evaporation (B), at $c_{HAP, p} = 1$ g/kg rock, 75°C, and at various values of P_{CO2} . All solution concentrations and solution I.S. are reported in log_{10} of molal units. Komatiite mineralogy is reported in Table 1.

EW = end-of-weathering; EE = end-of-evaporation; I.S. = ionic strength; P_{CO2} = partial pressure of atmospheric CO₂.

Comparing EW and EE systems, both show similar trends in terms of changes in secondary minerals precipitated and reversal in the $\text{Ca}^{2+}/\text{Mg}^{2+}$ ratio at a threshold value of $P_{\text{CO}2}.$ However, the behavior of secondary HAP is different: it is precipitated under all $P_{\text{CO}2}$ values during weathering, but it is not precipitated at any $P_{\text{CO}2}$ during evaporation. Hence, after evaporation, $\text{Mg}_T,$ $\text{Ca}_T,$ and Fe_T decrease relative to their EW values, whereas P_T increases.

3.1.3. The geochemical divide. We have seen above that a different suite of minerals and a reversal of the ${\rm Ca^{2+}/Mg^{2+}}$ ratio occur at some specific value of ${\rm P_{CO2}}$. The chemical evolution of the solutions at 75°C can be examined in detail during the weathering reaction path (Fig. 6a, c) and during the evaporation reaction path in terms of relative element enrichments (Fig. 6b, d). Each datum point on the ternary diagram represents the solution composition at the corresponding step in the reaction path. The first datum point

represents ξ =0 and the final point represents ξ =1. The HPO₄²⁻-Mg²⁺-Ca²⁺ ternary diagrams for both weathering (Fig. 6a) and evaporation (Fig. 6b) show HPO₄²⁻ enrichment, and much greater HPO₄²⁻ enrichment is achieved during evaporation at all values of P_{CO2}.

Furthermore, the solution becomes increasingly depleted in ${\rm Mg^{2^+}}$ and increasingly enriched in ${\rm Ca^{2^+}}$ at ${\rm P_{CO2}}{=}{\rm PAL}$ during both weathering and evaporation (Figs. 6a, b). The solution evolves similarly at ${\rm P_{CO2}}{=}0.005$ atm although the relative amount of ${\rm Mg^{2^+}}$ depletion is less than at PAL. By ${\rm P_{CO2}}{=}0.05$ atm, the solution evolves in the opposite direction, becoming more enriched in ${\rm Mg^{2^+}}$ and almost completely depleted in ${\rm Ca^{2^+}}$ as the reaction path proceeds before again moving away from the ${\rm Mg^{2^+}}$ enrichment towards phosphate enrichment. The difference in behavior between ${\rm Mg^{2^+}}$ and ${\rm Ca^{2^+}}$ is also seen in the ${\rm HCO_3^-}{-}{\rm Mg^{2^+}}{-}{\rm Ca^{2^+}}$ ternary diagram for weathering at ${\rm P_{CO2}}{=}0.005$ atm (Fig. 6c).

FIG. 4. Komatiite weathering reaction paths at 75°C and various P_{CO2} values. Komatiite containing $c_{HAP, p} = 1 \text{ g/kg}$ of rock is weathered. Reaction progress variable (ξ) is shown on the x axis and it varies from $\xi = 0$ at the start of the reaction path calculation to $\xi = 1$ at the end of the reaction path calculation. At completion of the reaction ($\xi = 1.0$), the reaction has proceeded to 5% of weathering. Secondary minerals precipitated as a result of weathering are shown in the left column. The corresponding fluid concentrations of selected free ions (Mg^{2+} , Ca^{2+} , Fe^{2+} , HPO_4^{2-} , and HCO_3^{-}) are shown in the right column. Compare with Fig. 11 for komatiite weathering at 25°C. See corresponding Supplementary Fig. S2 for tonalite weathering at 75°C.

.001

Komatiite Weathering, 75 °C PAL HCO3 .01 Some fluid components (mol) .001 .01 Minerals (mol) .4 .5 .6 Rxn progress Rxn progress EW solution Saponite-Mg **10 X PAL** HCO2 .01 Some fluid components (mol) Saponite-Na Minerals (mol) Hydroxyapatite Caolinite 1e-7 1e-6 1e-7 1e-9 4 .5 Rxn progress 1e-10 Rxn progress 0.5 atm Chalcedony Magnesite HCO₃ Dolomite-ord Mg⁺⁺ Some fluid components (mol) Minerals (mol) .001 Hydroxyapatite 1e-6 Rxn progress A .5 ... Rxn progress MagnesiteChalcedony HCO3 5 atm Dolomite-ord Some fluid components (mol) .01 Mg++ Minerals (mol)

Rxn progress

Hydroxyapatite

.4 .5 .6 Rxn progress

Komatiite Evaporation, 75 °C

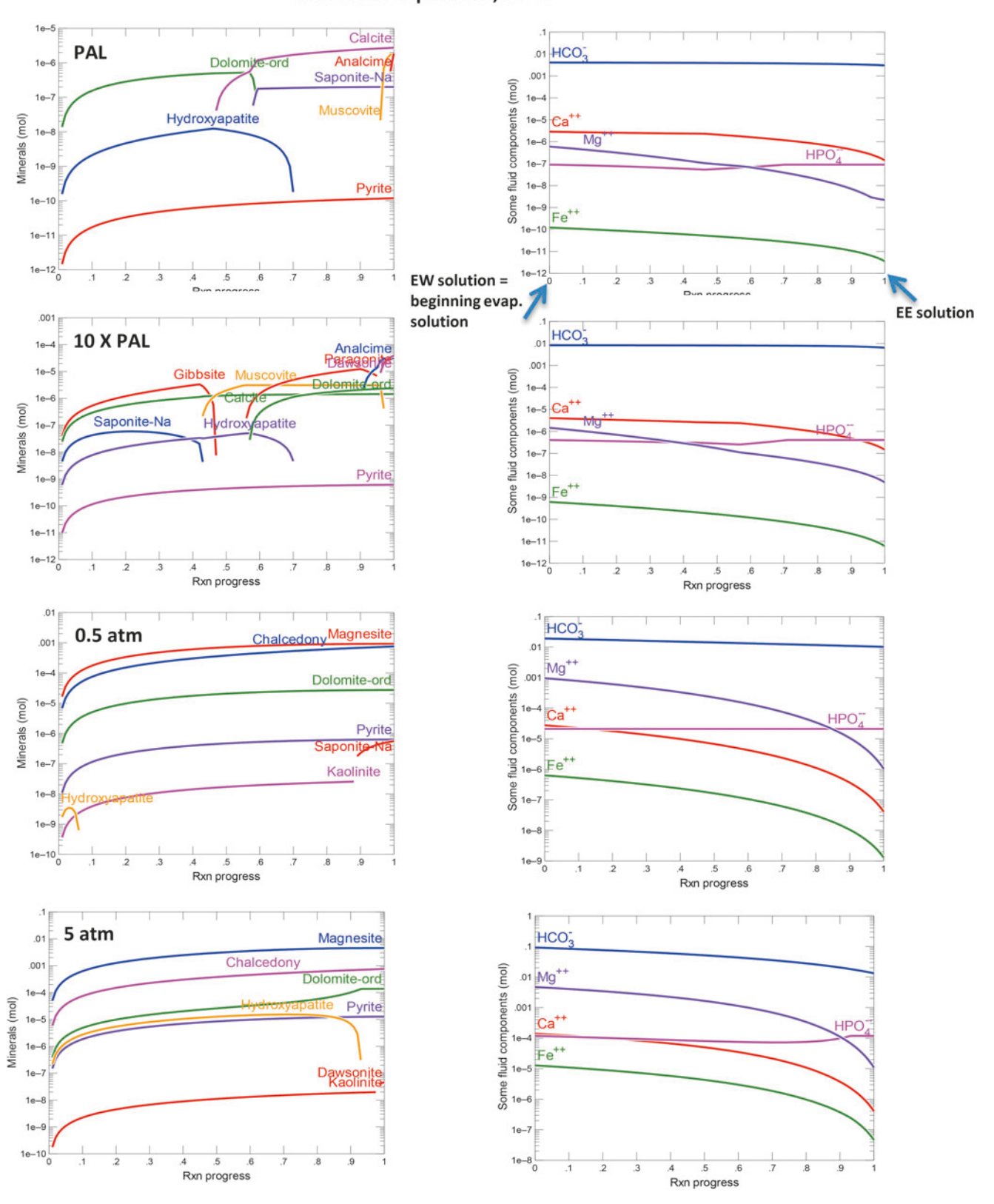


FIG. 5. Evaporation reaction paths of komatiite-weathering-generated solutions at 75°C and various P_{CO2} values. One cycle of evaporation. Reaction progress variable (ξ) is shown on the x axis and it varies from $\xi = 0$ at the start of the reaction path calculation to $\xi = 1$ at the end of the reaction path calculation. At completion of the reaction ($\xi = 1.0$), the reaction has proceeded to 95% of evaporation. Secondary minerals precipitated as a result of evaporation are shown in the left column. The corresponding fluid concentrations of selected free ions (Mg^{2+} , Ca^{2+} , Fe^{2+} , HPO_4^{2-} , and HCO_3^{-}) are shown in the right column. Compare with Fig. 13 for komatiite weathering at 25°C. See corresponding Supplementary Fig. S3 for tonalite evaporation at 75°C.

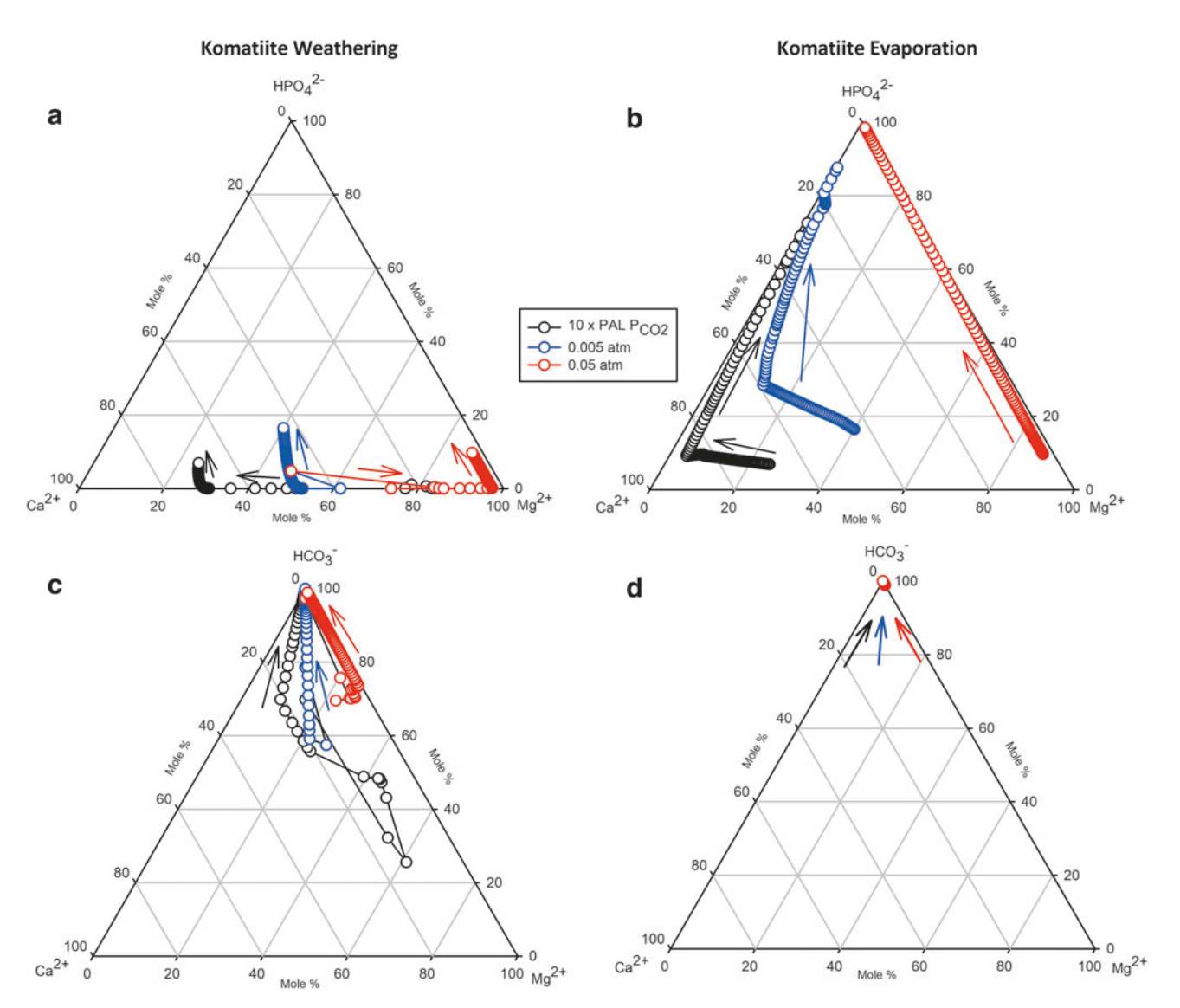


FIG. 6. Evolution of solution composition during komatiite weathering (left panel: **a, c**) and evaporation (right panel: **b, d**) reaction paths at 75°C at various P_{CO2} values shown as ternary diagrams. The upper panels show HPO_4^{2-} , Ca^{2+} , and Mg^{2+} concentrations (mole %) at the apices of the ternary plots (**c, d**). A geochemical divide emerges between Ca and Mg in both the phosphate and the carbonate ternary diagrams during the weathering reaction path (**a, c**) and only in the phosphate ternary diagram during the evaporation reaction path (**b, d**). Starting composition for the evaporation reaction path was the komatiite (cHAP, p=1 g/kg komatiite) EW solution at various PCO2s and T=75°C. Data points represent each step of the reaction progress variable (ξ =0-1 values on *x* axis of Figs. 4 and 5, respectively). Arrows indicate direction of evolution of the solution composition during the reaction path. Compare with Fig. 15 for tonalite results at 75°C. T, temperature.

This interesting divergence as $P_{\rm CO2}$ increases above a certain threshold can be explained by the "geochemical divide" principle (Hardie and Eugster, 1970). According to this principle, the initial ion ratios of the solution exquisitely control the precipitation sequence of minerals as the komatiite weathers, and thus, the final ion concentrations. In the present situation, a geochemical divide is shown to develop between calcium and magnesium. As a result, the relative enrichment of these two elements changes at the geochemical divide defined by a critical value of $P_{\rm CO2}$.

At higher values of P_{CO2} , the starting solution created by reacting pure rainwater with atmospheric gases and rock is very highly enriched in HCO_3^- and is highly acidic with pH $\sim 2-3$. This corresponds to the beginning of the reaction

path model. After the first step of the weathering reaction path occurs, there is more HCO_3^- (2.05×10^{-3} molal) than dissolved silica ($SiO_{2(aq)} = 8 \times 10^{-4}$ molal), and hence, carbonates predominate over metal aluminosilicates. Precipitation of Ca- and Mg- carbonates does not leave sufficient metals for the formation of metal aluminosilicates (including Mg-saponite), such that the dissolved silica and dissolved aluminum are precipitated out as chalcedony and pure aluminosilicate (kaolinite) (Fig. 4).

Furthermore, at the first step of the weathering reaction path, a calcium phase (HAP) forms and depletes the solution in Ca²⁺and relatively enriches it in Mg²⁺ (Fig. 4). Subsequently, saturation with dolomite and magnesite is reached, such that the solution composition moves away from the Mg apex toward

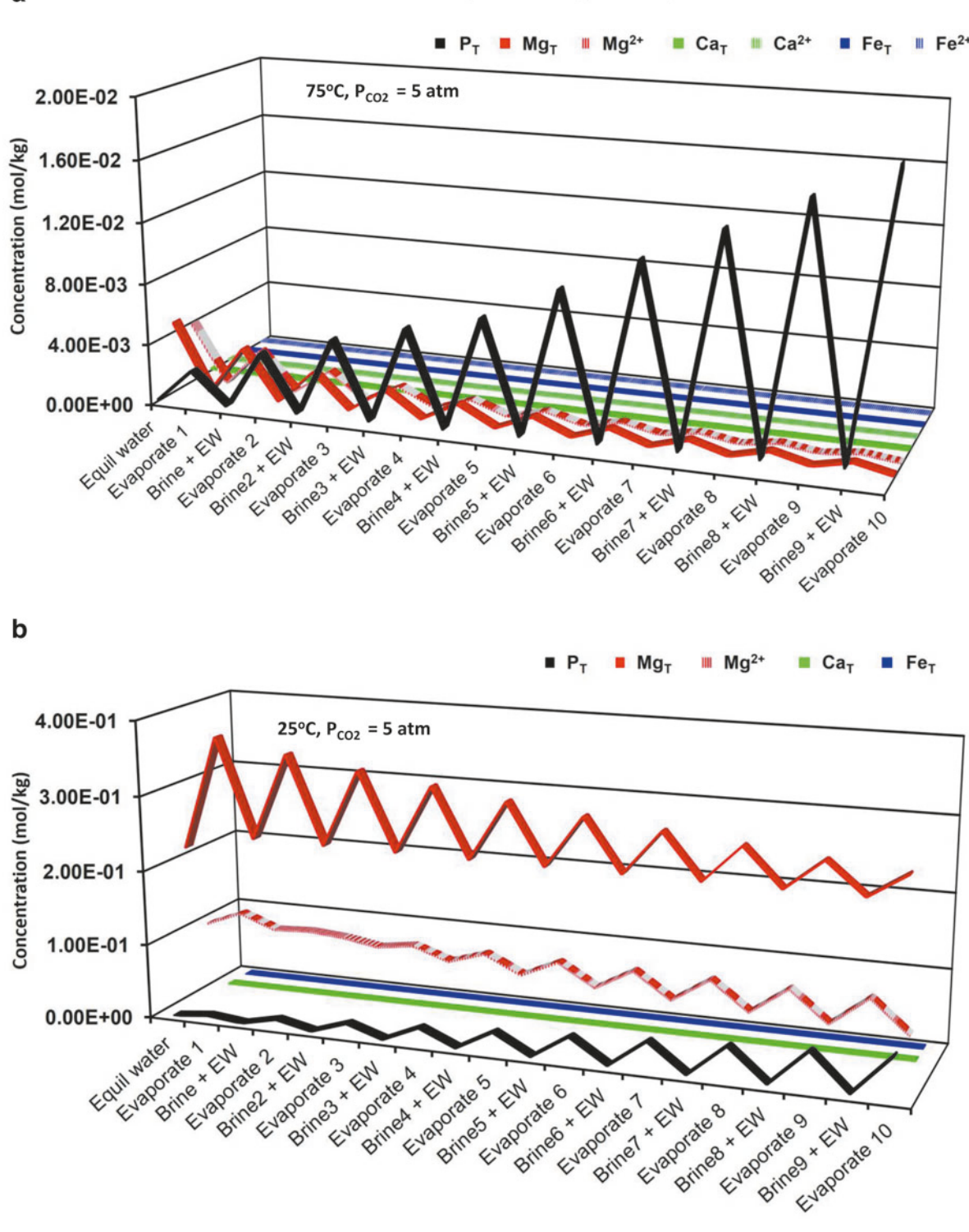


FIG. 7. Solution chemistry produced after 10 cycles of evaporation-rehydration in the komatiite system ($c_{HAP, p} = 1 \text{ g/kg}$ komatiite) at $P_{CO2} = 5$ atm and (a) $T = 75^{\circ}\text{C}$ or (b) $T = 25^{\circ}\text{C}$. Final total dissolved concentrations of phosphate, magnesium, calcium and iron (II) and the free ion concentrations (all in molal units) are reported on the y axis for values $> 1 \times 10^{-8}$ molal (see sections 3.1.1-3.1.4 for explanation). Carbonate, silicate, aluminosilicate minerals and pyrite precipitation depletes the cations at each evaporative step, while phosphate accumulates because HAP does not precipitate at each evaporation step. Rehydration with fresh solution derived from weathering replenishes cation and phosphate concentrations. Ultimately, high phosphate concentrations can be achieved with an increasing number of cycles. Note that the relative concentrations of phosphate and magnesium change upon decreasing temperature from 75°C to 25°C.

 $\mathrm{HPO_4}^{2-}$ enrichment (Fig. 6). In contrast, the initial solution is less $\mathrm{HCO_3}^-$ rich and less acidic at lower $\mathrm{P_{CO2}}$ values. Hence, metal aluminosilicates (saponite and amesite) and aluminum hydroxide (gibbsite) form along with carbonates (ordered dolomite) (Fig. 4). Since Mg-saponite and amesite precipitation depletes the solution in $\mathrm{Mg^{2+}}$ and enriches it in $\mathrm{Ca^{2+}}$, the solution moves toward the $\mathrm{Ca^{2+}}$ apex (Fig. 6).

The solution compositions at the end of the weathering reaction path $(\xi=1)$ become the starting solution compositions for the evaporation reaction path (e.g.), the final points in any of the trajectories in Fig. 6a or c are the starting points for trajectories in Fig. 6b or d, respectively). The changes in the suites of secondary minerals formed (Fig. 5a) and the reversal in the aqueous Ca^{2+}/Mg^{2+} ratio at a threshold P_{CO2} value (Figs. 5b and 6b, d) are also seen in the EE solutions, which explains the EE solution evolution toward Ca^{2+} or Mg^{2+} apices of the ternary diagram (Fig. 6). Different from EW solutions, however, is that no HAP is precipitated during evaporation (Fig. 4 versus Fig. 5), and so, the solutions move toward the HPO₄²⁻ apex much more dramatially than in the EW ternary diagram (Fig. 6b vs. 6a).

3.1.4. Cyclic wetting and drying. The nature of evaporative environments is not to undergo just one evaporative cycle but, rather, multiple drying and wetting events (Fig. 1). The EW solution from komatiite was subjected to 10 cycles of 95% evaporation and rehydration at 75°C (Fig. 7, Supplementary Table S1, and Fig. 8a; see Section 2. Methods). There is not a very large increase in total dissolved element concentrations as $P_{\rm CO2}$ increases from 0.5 to 5 atm. At all $P_{\rm CO2}$ values, $P_{\rm T}$ increases, while Mg_T, Ca_T, and Fe_T decrease with an increasing number of evaporation and rehydration cycles (Figs. 7 and 8). This trend is seen because phosphate is not removed during evaporation (no HAP precipitation) and additional dissolved phosphate is added during each rehydration step, whereas the other elements are removed at each evaporation step by precipitation of other mineral phases.

The total dissolved element concentrations decrease as $P_T > Mg_T > Ca_T > Fe_T$ at 75°C. In detail, P_T builds up from ~ 0.1 mmolal level and reaches > 10 mmolal level, while Mg_T decreases from ~ 0.1 mmolal to $10\,\mu$ molal level, Ca_T decreases from micromolal to $0.1\,\mu$ molal level, and Fe_T decreases from about micromolal to 10 nmolal. P_T is close to and even exceeds the biological level (1 mmolal) at all $P_{CO2} = 0.5 - 5$ atm, but all the other elements are below biological levels (green lines in Fig. 8a).

Significantly, we have identified empirical relationships between the total dissolved concentrations and the evaporation-rehydration cycle number (Supplementary Fig. S1 and Supplementary Table S2). At each $P_{\rm CO2}$, $P_{\rm T}$ increases linearly with the number of rehydration/evaporation cycles, and $Mg_{\rm T}$, $Ca_{\rm T}$, and $Fe_{\rm T}$ demonstrate power law dependence on cycle number. For example, at $P_{\rm CO2}$ =5 atm and T=75°C, $P_{\rm T}$ =1 molal after 555 rehydration/evaporation cycles. After this number of cycles, the empirical regressions

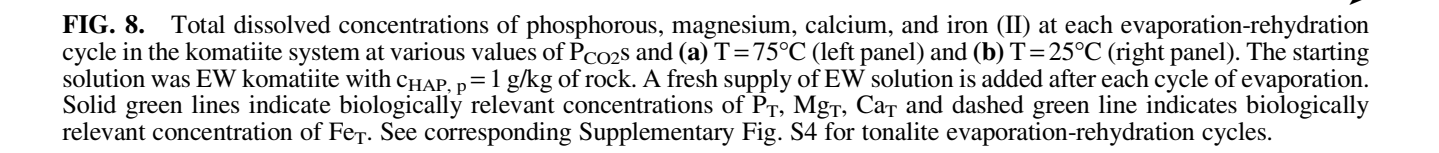
provide estimates of the $Mg_T \sim 0.4 \,\mu molal$, $Ca_T \sim 8$ nmolal, and $Fe_T \sim 0.5$ nmolal. In contrast, an unrealistic 500,000 cycles would be needed at PAL to achieve $P_T = 1$ molal.

3.1.5. Magnesium speciation. Most reports on magnesium concentrations in biological systems (Milo and Phillips, 2015) and nonenzymatic nucleotide polymerization cite the total dissolved magnesium concentration because of the difficulty in determining the precise speciation in complex systems. Here, we focus briefly on magnesium speciation at 75°C in the cyclical evaporation-rehydration systems because the concentration of the free uncomplexed ion changes significantly in the system with the number of cycles (Fig. 9a). In almost all the systems, the dominant ion is not free Mg²⁺ but, rather, aqueous carbonate complexes. MgHCO₃⁻ and MgCO₃⁰ are the dominant ions at lower P_{CO2} values (0.5 and 1 atm), but MgHCO₃⁻ and Mg²⁺ become dominant at higher P_{CO2} values (≥ 2 atm); MgSO₄⁰ and MgHPO₄⁰ are in very low abundance in most systems. The influence of these subtle changes in Mg speciation on RNA polymerization may be potentially significant, especially for RNA templated and RNA-primer mediated polymerization. In contrast, montmorillonite-promoted RNA polymerization, which can proceed at low (~5 mM Mg_T) or even in the total absence of Mg²⁺ especially when cocatalyzed by amino acids (Kaddour et al., 2018; Namani et al., 2021), would be much less affected by changes in magnesium speciation.

3.1.6. Temperature effects on solutions resulting from komatiite weathering and evaporation. We tested the effects of temperature from 25°C to 75°C on solution composition after weathering at various values of P_{CO2} , and the total dissolved element concentrations are reported in Fig. 10. Reactions paths for weathering at $T=25^{\circ}C$, $P_{CO2}=PAL$, or 5 atm are shown in terms of secondary minerals precipitated and evolution of solution composition (Fig. 11). Total dissolved element concentrations after one cycle of evaporation at $T=25-75^{\circ}C$ and at various values of P_{CO2} were also determined (Fig. 12). Evaporation reaction paths at $T=25^{\circ}C$, $P_{CO2}=PAL$, or 5 atm are shown in terms of minerals precipitated and evolution of solution composition (Fig. 13).

Results at 25°C after 10 cycles of rehydration-evaporation for total dissolved element concentrations (Fig. 8b) and magnesium speciation (Fig. 9b) can be compared with those obtained at 75°C (Figs. 8a and 9a, respectively). EW and EE solution compositions at $P_{\rm CO2}$ =PAL and 5 atm and T=25°C are reported in Supplementary Table S3.

At PAL, comparing 25°C and 75°C in EW solutions, the same minerals are formed at both temperatures, except that gibbsite is no longer stable at a higher temperature and, instead, Na-saponite and Ca-saponite appear (Fig. 11 left panel vs. Fig. 4 left panel). The concentration of most of the ions (Mg²⁺, Ca²⁺, HPO₄²⁻), except HCO₃⁻ and Fe²⁺, is lower as the temperature increases (Fig. 11 right panel vs.



Komatiite: Evaporation-Rehydration Cycles a b 75°C 25°C 100 10-2 PAL, 25 °C PAL, 75°C 10-3 10-1 10-4 10-2 10-5 10-3 Concentration (mol/kg) Concentration (mol/kg) 10-6 10-4 10-7 10-5 10-8 10-6 10-9 10-7 10-10-10-8 10-11. 10-9 10-12-10-10 10-13-10-1 10-14 10-12 10-15. 10 10 Evaporation cycle # Evaporation cycle # 10° 10° 0.5 atm, 75°C 10-1 10-1 10-2 10-2 10-3 10-3 Concentration (mol/kg) Concentration (mol/kg) 10-4 10-4 0.5 atm. 25°C 10-5 10-5 10-6 10-6 10-7 10-7 **─** Mg⊤ 10-8 -10-8 - CaT Fe_T 10-9 -10-9 10-10 10-10 10-11 10-11 10-12 10-12 6 5 Evaporation cycle # Evaporation cycle # 10° 10° 1 atm, 75°C 10-1 10-1 10-2 10-2 10-3 10-3 Concentration (mol/kg) Concentration (mol/kg) 10-4 10-4 10-5 10-5 10-6 10-6 10-7 10-7 10-8 10-8 10-9 10-9 1 atm, 25°C 10-10 10-10 10-11 10-11 10-12 10-1 5 10 5 Evaporation cycle # Evaporation cycle # 100 10° 5 atm, 75°C 10 10-1 10-2 10-2 10-3 10-3 Concentration (mol/kg) Concentration (mol/kg) 10-4 10-4 10-5 10-5 10-6 10-6 10-7 10-7 10-8 10-8 5 atm, 25°C 10-9 10-9 10-10 10-10 10-11 10-1 10-12 10-12 2 5 6 8 9 10 6 9 10

Evaporation cycle #

Evaporation cycle #

Komatiite Evaporation-Rehydration Cycles: Mg speciation

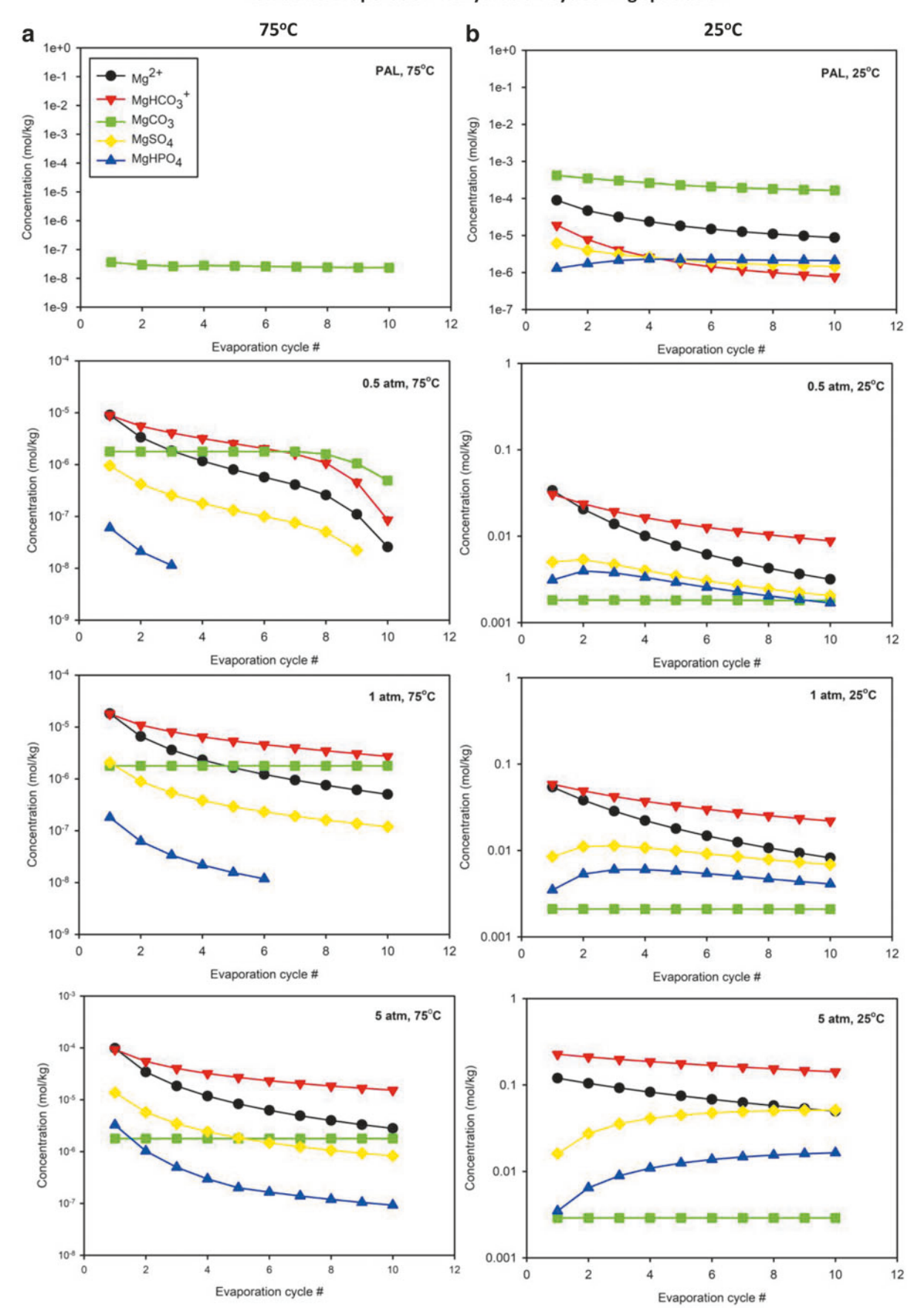


FIG. 9. Magnesium speciation at each cycle of evaporation and rehydration up to 10 cycles at various values of P_{CO2} and (a) $T=75^{\circ}C$ (left panel) and (b) $25^{\circ}C$ (right panel). The starting solution was EW komatiite ($c_{HAP, p}=1$ g/kg of rock). A fresh supply of EW solution is added after each cycle of evaporation. The total magnesium for these systems is shown in Fig. 8.

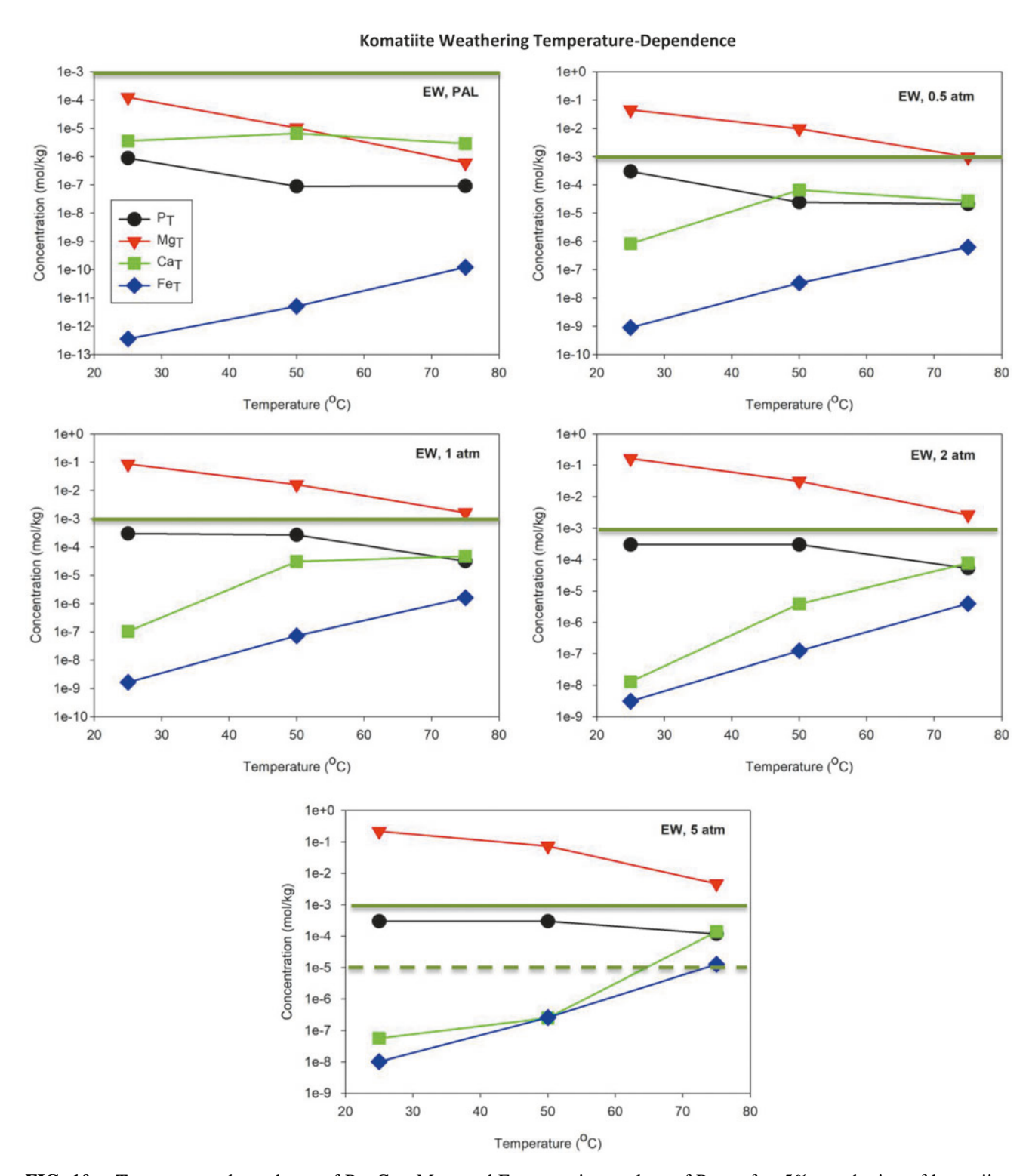


FIG. 10. Temperature dependence of P_T , Ca_T , Mg_T , and Fe_T at various values of P_{CO2} after 5% weathering of komatiite. Komatiite containing $c_{HAP, p} = 1$ g/kg of rock is weathered. Solid green lines indicate biologically relevant concentrations of P_T , Mg_T , Ca_T and dashed green line indicates biologically relevant concentration of Fe_T . See Supplementary Fig. S5 for the corresponding tonalite results.

Fig. 4 right panel). This trend is observed because all the phases formed at 25°C (disordered dolomite, HAP, gibbsite, amesite, and saponite) have retrograde solubility (*i.e.*, less soluble as temperature increases); therefore, there is less Mg²⁺, Ca²⁺, HPO₄²⁻ in solution but more HCO₃⁻ because of less carbonate precipitation at a higher temperature. The

exception is pyrite, which becomes more soluble as temperature increases, resulting in more Fe²⁺ in solution.

At higher P_{CO2} values, such as 5 atm, the minerals formed are similar (chalcedony, carbonates, pyrite, and kaolinite) at $T=25^{\circ}$ C and at 75°C in EW solutions (Figs. 10 and 11 vs. Fig. 4). The only difference is that HAP is not formed at

Komatiite Weathering, 25 °C

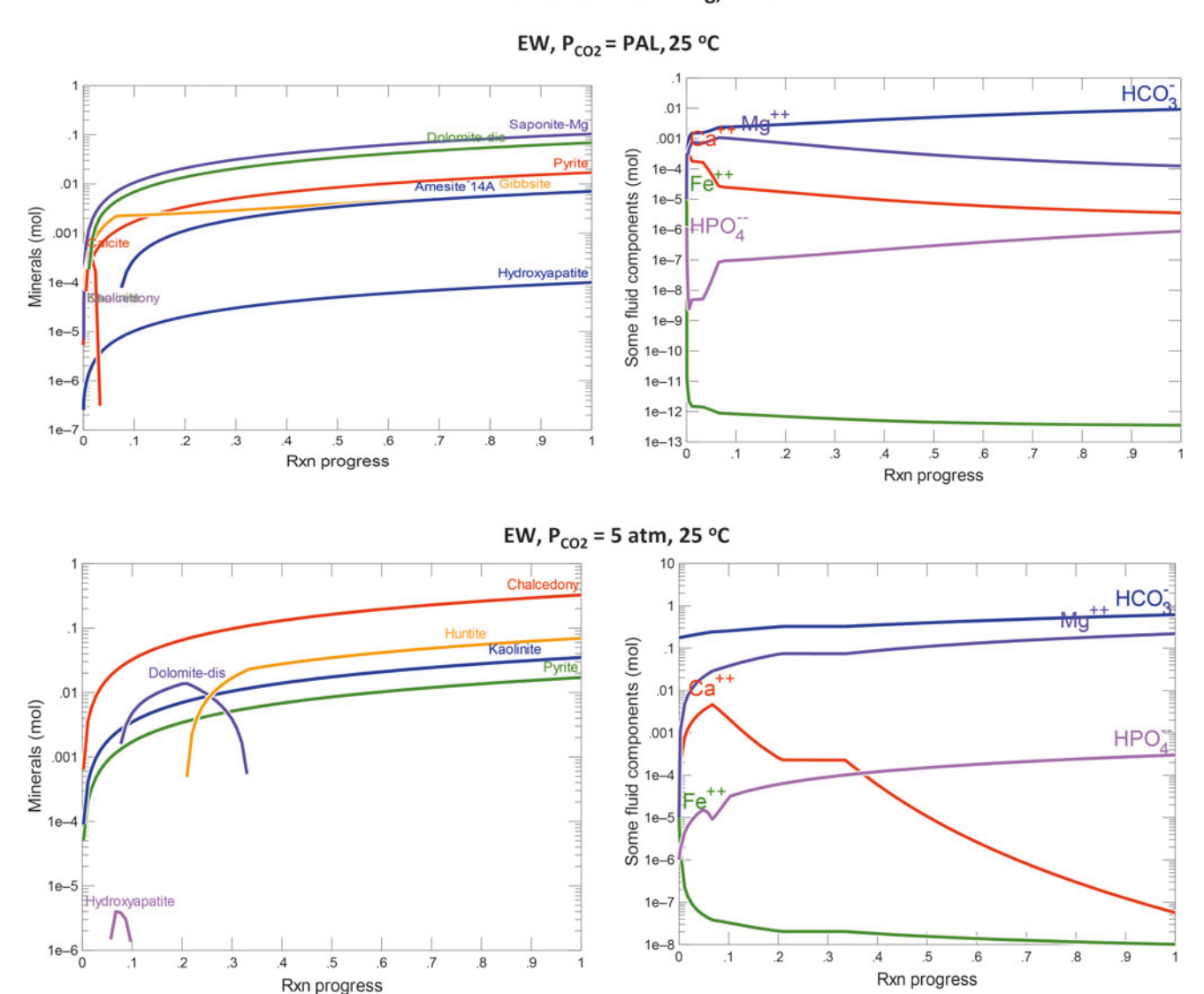


FIG. 11. Komatiite weathering reaction paths at 25°C and at P_{CO2} =PAL or 5 atm. Komatiite containing $c_{HAP, p}$ = 1 g/kg of rock is weathered. Reaction progress variable (ξ) is shown on the x axis and it varies from ξ = 0 at the start of the reaction path calculation to ξ = 1 at the end of the reaction path calculation. At completion of the reaction (ξ = 1.0), the reaction has proceeded to 5% of weathering. Secondary minerals precipitated as a result of weathering are shown in the left column. The corresponding fluid concentrations of free ions, Mg^{2+} , Ca^{2+} , Fe^{2+} , HPO_4^{2-} , and HCO_3^{-} , are shown in the right column. Compare with Fig. 4 for results at 75°C. PAL, present atmospheric level.

25°C, but precipitates at 75°C during weathering. The decrease in concentrations of Mg²⁺ and HPO₄²⁻ and the increase in HCO₃⁻ concentration as temperature increases are related to the retrograde solubility of the Mg-bearing minerals, including saponite, and HAP. The concentration of Fe²⁺ increases because of increasing solubility of pyrite with temperature. The concentration of Ca²⁺ increases with temperature in systems where huntite is formed at 25°C but is replaced by dolomite at higher temperatures.

The EE systems show similar trends in terms of solution compositions and secondary minerals formed at each $P_{\rm CO2}$ and temperature (Figs. 12 and 13) as their corresponding EW counterparts (Figs. 10 and 11). Cyclical evaporation and rehydration at 25°C show similar trends to those seen at 75°C with increasing $P_{\rm T}$ and decreasing $M_{\rm gT}$, $Ca_{\rm T}$, and $Fe_{\rm T}$ as the number of cycles

increases (Fig. 7b and Supplementary Table S4). Again, fitting a linear equation to P_T as a function of cycle number suggests that, at $P_{CO2} = 5$ atm, $P_T = 1$ molal is achieved after 175 cycles. At this number of cycles, the empirical regressions predict estimates of $Mg_T = 0.18$ molal, while Ca_T and Fe_T are below nanomolar levels. Similar to the 75°C result, 500,000 cycles are required to achieve $P_T = 1$ molal at PAL and 25°C.

In summary, P_T and Mg_T are greater at lower temperatures and decrease with increasing temperature and the opposite trend is seen for Ca_T and Fe_T in both weathering and evaporating solutions (Figs. 10 and 12).

3.1.7. Sulfur redox sensitivity analyses varying at P_{CO2} =5 atm and T=75°C. For sulfur redox states, sensitivity analysis of P_{H2S} over eight orders of magnitude from

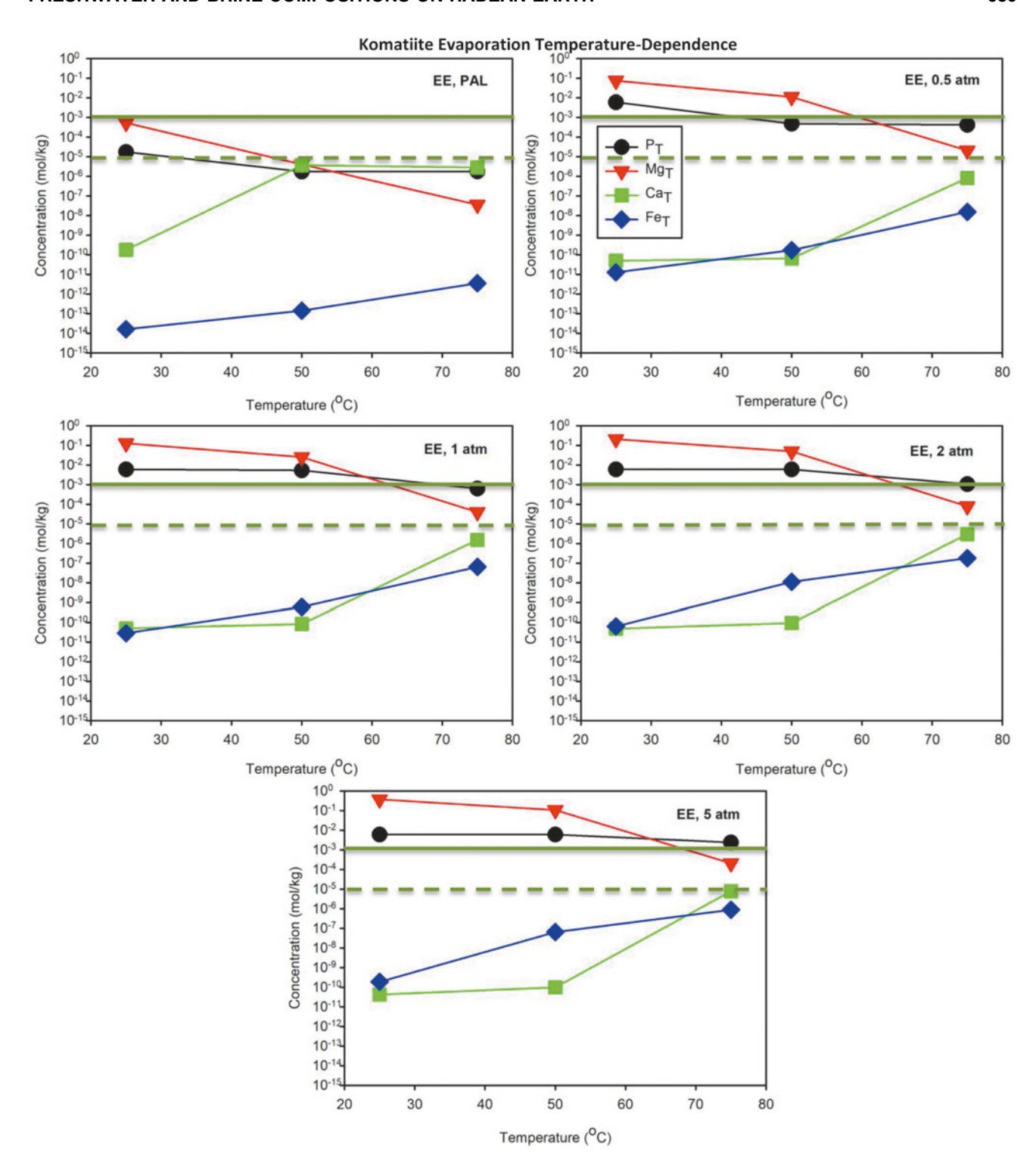


FIG. 12. Temperature dependence of P_T , Ca_T , Mg_T , and Fe_T at various values of P_{CO2} after one cycle of evaporation. The starting solution was EW solution of komatiite ($c_{HAP, p} = 1$ g/kg of rock). Solid green lines indicate biologically relevant concentrations of P_T , Mg_T , Ca_T and dashed green line indicates biologically relevant concentration of Fe_T . See Supplementary Fig. S5 for tonalite results.

0.25 to 1×10^{-9} atm and of aqueous SO_4^{2-} concentration from 200 mM to 1 M showed little effect (within only one order of magnitude) on total phosphorus, total Mg, and total calcium in komatiite EW and EE solutions. However, total Fe concentrations increased as P_{H2S} decreased and aqueous SO_4^{2-} concentrations decreased.

3.2. Subaerial weathering of tonalite and subsequent evaporation

3.2.1. Weathering. Subaerial partial weathering at 75° C of tonalite containing 1 g HAP/kg of rock results in decreasing pH from alkaline (pH \sim 9) at PAL to acidic (pH

Komatiite Evaporation, 25 °C

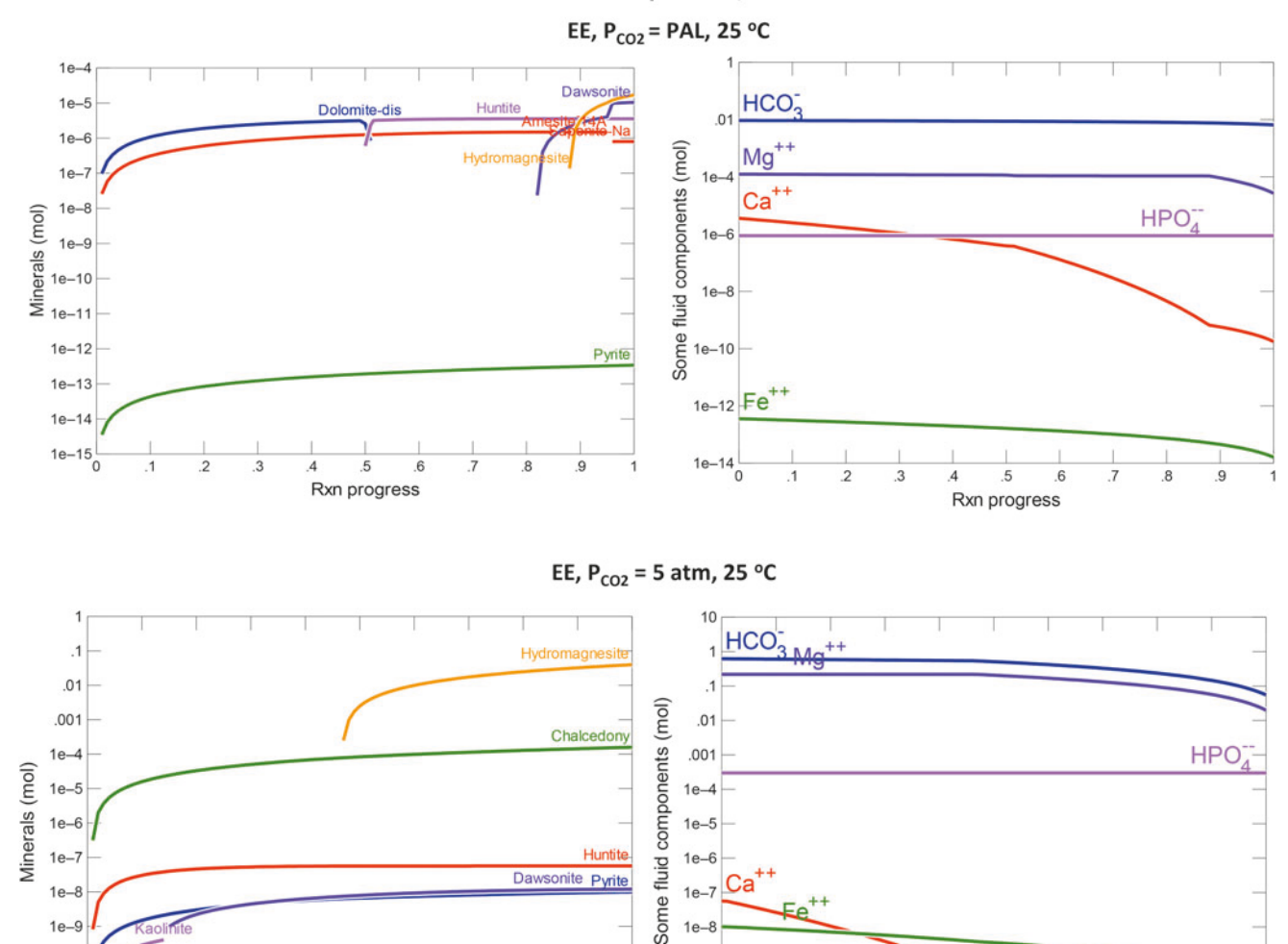


FIG. 13. Evaporation reaction paths of komatiite-weathering-generated solutions at 25°C and P_{CO2} =PAL or 5 atm. Once cycle of evaporation of EW solution. Reaction progress variable (ξ) is shown on the x axis and it varies from ξ =0 at the start of the reaction path calculation to ξ =1 at the end of the reaction path calculation. At completion of the reaction (ξ =1.0), the reaction has proceeded to 95% of evaporation. Secondary minerals precipitated as a result of evaporation are shown in the left column. The corresponding fluid concentrations of free ions, Mg^{2+} , Ca^{2+} , Fe^{2+} , HPO_4^{2-} and HCO_3^- , are shown in the right column. Compare with Fig. 5 for komatiite weathering at 75°C.

 \sim 6) at P_{CO2} =5 atm, and greater values of P_T , Mg_T , Ca_T , and Fe_T as P_{CO2} increases (Fig. 14 and Table 3). These trends are similar to those obtained for komatiite weathering (Fig. 2). At PAL, element concentrations are on the same order of magnitude as for komatiite; but at P_{CO2} =5 atm, tonalite weathering results in significantly lower P_T , Mg_T , and Fe_T , whereas Ca_T is in the same order of magnitude as for komatiite. Increasing the HAP content of the tonalite to $10\,g$ HAP/kg of rock did not affect the solution composition (Fig. 14).

Rxn progress

At $P_{CO2} \le 10 \times PAL$, the secondary minerals formed are aluminosilicates (analcime, Ca-clinoptilolite, Ca-saponite, muscovite, and paragonite), calcite, pyrite, and HAP (Table 1 and Supplementary Fig. S2). At $P_{CO2} \ge 0.5$ atm, fewer

aluminosilicates are formed, including saponite not forming; instead, ordered dolomite, chalcedony, kaolinite, pyrite, and HAP are precipitated. The change in the suite of minerals with increasing $P_{\rm CO2}$ values is similar to that observed for komatiite weathering. Saponites (Mg-enriched clay) chiefly control Mg^{2+} ion concentration at lower values of $P_{\rm CO2}$ and ordered dolomite plays this role at higher $P_{\rm CO2}$ values.

Rxn progress

3.2.2. Evaporation. Concentrations of all elements except phosphorus decrease after a single evaporation cycle (Fig. 14, Table 3, and Supplementary Table S5, first row of data corresponds to evaporation cycle 1 solution at each $P_{\rm CO2}$ value). The trends with respect to pH and element

Tonalite: Weathering and Evaporation, 75 °C

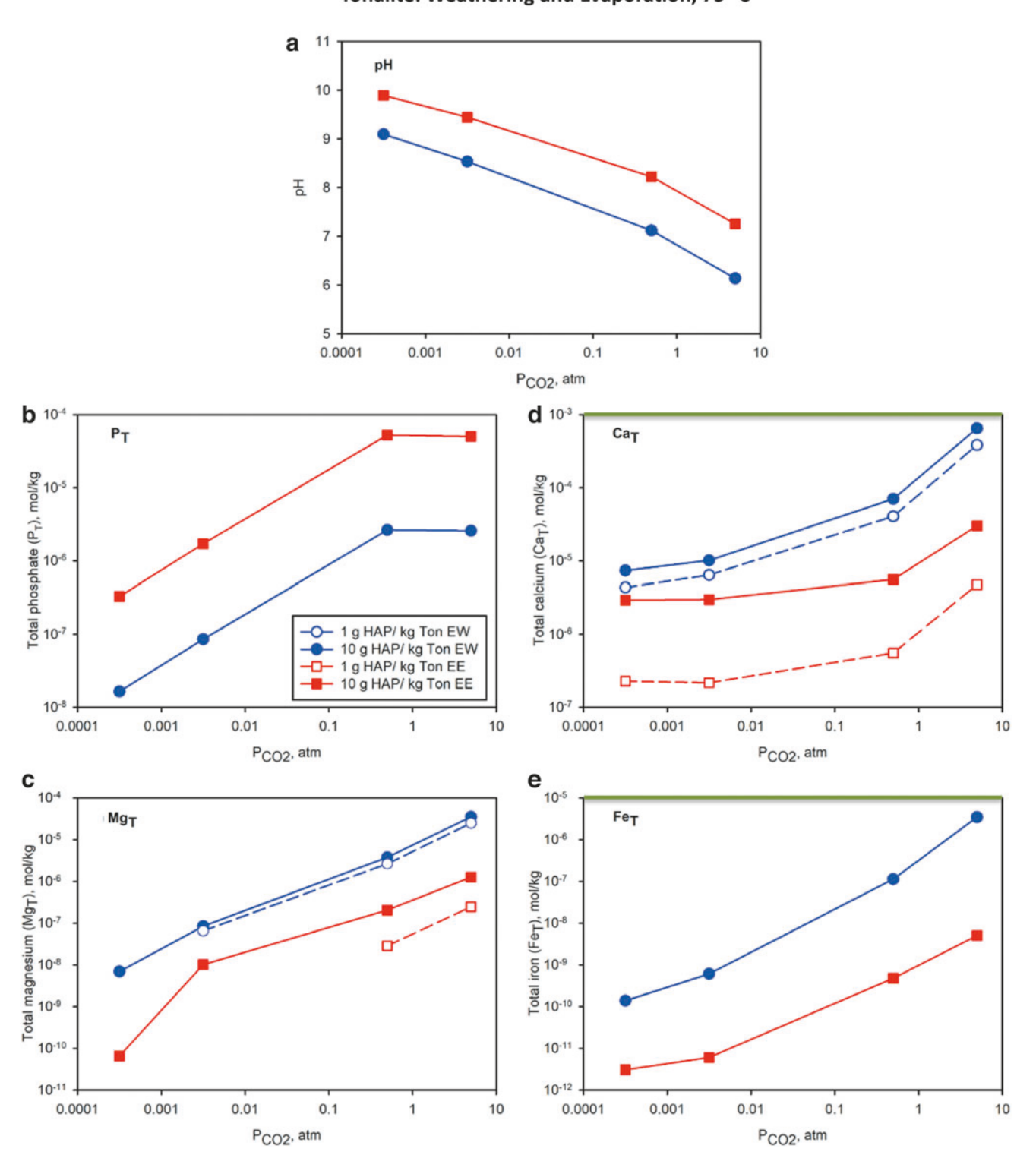


FIG. 14. Tonalite (ton) EW (blue symbols) and EE (red symbols) solution chemistry at 75°C as a function of various values of P_{CO2} for tonalite containing with low and high primary HAP content ($c_{HAP, p}$) (empty and filled symbols, respectively). (a) pH and concentrations (molal) of (b) total phosphate (P_{T}), (c) total magnesium (P_{T}), (d) total calcium (P_{T}), and (e) total iron (P_{T} = P_{T} = P_{T} = P_{T}). Solid green lines indicate biologically relevant concentrations of P_{T} , P_{T} = $P_$

| | | | | | | ~ | | | |
|-----------------------|----------------|-----------|-------|--------|-----------|--------|--------|-----------|-------|
| P_{CO2} (atm) | pН | I.S. | P_T | Mg_T | Mg^{2+} | Fe_T | Ca_T | Ca^{2+} | C_T |
| (A) EW concent | tration log | (molal) | | | | | | | |
| 3.16×10^{-4} | 9 | -2.29 | -7.78 | -8.16 | n.d. | -9.86 | -5.13 | -5.36 | -2.50 |
| 3.16×10^{-3} | 8.5 | -2.01 | -7.07 | -7.07 | -7.19 | -9.21 | -5.00 | -5.19 | -2.08 |
| 0.5 | 7.1 | -1.25 | -5.58 | -5.42 | -5.58 | -6.95 | -4.15 | -4.39 | -1.20 |
| 5 | 6.1 | -1.23 | -5.59 | -4.45 | -4.60 | -5.46 | -3.19 | -3.42 | -0.88 |
| (B) EE concentr | ation \log_1 | 0 (molal) | | | | | | | |
| 3.16×10^{-4} | 9.8 | -0.94 | -6.48 | -10.18 | n.d. | -11.51 | -5.54 | -6.64 | -1.32 |
| 3.16×10^{-3} | 9.4 | -0.66 | -5.77 | -7.99 | n.d. | -11.21 | -5.53 | -6.66 | -0.89 |
| 0.5 | 8.2 | -0.01 | -4.28 | -6.69 | -7.54 | -9.32 | -5.25 | -6.26 | 0.03 |
| 5 | 7.2 | -0.03 | -4.30 | -5.90 | -6.61 | -8.30 | -4.52 | -5.32 | 0.07 |

Table 3. Tonalite Weathering and Evaporation Solution Chemistry at 75°C and Various Partial Pressures of CO₂

Solution pH and concentrations of total phosphate (P_T) , total magnesium (Mg_T) , free magnesium ion (Mg^{2^+}) , total iron (Fe_T) , total calcium (Ca_T) , free calcium ion (Ca^{2^+}) , and total carbonate (C_T) after 5% weathering of tonalite (A) and after subjecting the EW solution to one cycle of 95% evaporation (B), at $c_{HAP,\ p}=1$ g/kg rock, 75°C, and various P_{CO2} s. All solution concentrations and solution I.S. are reported in log_{10} of molal units. Tonalite mineralogy is reported in Table 1.

concentrations were similar to those obtained in EW solutions (Table 3). Increasing the HAP content of the tonalite to $10 \,\mathrm{g}$ HAP/kg of rock did not affect the solution composition (Fig. 14). The changes in the mineralogy of the secondary minerals are broadly similar to those obtained in the komatiite EE solutions (Fig. 5), except that siderite (FeCO₃) replaces pyrite as the secondary Fe-mineral precipitated at $P_{CO2} = 5$ atm (Supplementary Fig. S2).

3.2.3. Ternary diagrams. The evolution of solution composition during tonalite weathering and evaporation reaction paths is shown in Fig. 15. No geochemical divide is seen (i.e., the $\text{Ca}^{2+}/\text{Mg}^{2+}$ ratio does not reverse) as P_{CO2} increases; precipitation of Ca-saponite and Ca-clinoptilolite at low P_{CO2} and dolomite at higher P_{CO2} values during the early stages of the reaction path (Supplementary Fig. S3) drives the solution compositions toward the Ca apex (Fig. 15a, c). During the evaporation step, the solution moves toward the HPO₄²⁻ apex (Fig. 15b, d), because HAP is not precipitated (Supplementary Fig. S3).

3.2.4. Cyclic wetting and drying. The EW solution from tonalite was subjected to 10 cycles of 95% evaporation and rehydration at 75°C (Supplementary Fig. S4a, left panel). At all values of $P_{\rm CO2}, P_{\rm T}$ increases, while $Mg_{\rm T}, Ca_{\rm T},$ and $Fe_{\rm T}$ decrease with the increasing number of evaporation and rehydration cycles. This trend is seen because phosphate is not removed during evaporation (no HAP precipitation) and additional dissolved phosphate is added during each rehydration step, whereas the other elements are removed at each evaporation step. The total dissolved element concentrations decrease as $P_{\rm T} >> Mg_{\rm T} > Fe_{\rm T}.$ At PAL, $Ca_{\rm T}$ is greater than or equal to $P_{\rm T}$ but becomes less than $P_{\rm T}$ at higher $P_{\rm CO2}$ (Supplementary Fig. S4a, left panel).

All values (Mg_T , Ca_T and Fe_T) are below 1 mmolal, except P_T , which approaches 1 mmolal at 5 atm and 10 cycles of evaporation. Fitting P_T to a linear equation dependent on the number of cycles yields P_T =1 molal after 20,000 cycles at 5 atm at T=75°C, and the total dissolved element concentrations of Mg, Ca, and Fe are subnanomolal (Supplementary Table S2). In contrast, at PAL, 3,333,333 cycles are needed to achieve P_T =1 molal.

Solution composition at 25°C with 10 cycles of evaporation and rehydration is shown in Supplementary Fig. S4b (right panel). In general, all concentrations are even lower

than at 75°C, except for Mg_T , which is greater because ordered dolomite is replaced by huntite as a major Mg_T mineral. At 25°C and $P_{CO2}=5$ atm, $P_T \sim 1$ mmolal, $Mg_T \sim 0.1$ molal, while Ca_T and Fe_T fall below 1 nmolal. At 25°C and PAL or $P_{CO2}=5$ atm, an even greater number of cycles is required than at 75°C (Supplementary Fig. S4b vs. S4a). Finally, comparing tonalite solution compositions (Supplementary Fig. S4) with those obtained from cyclical evaporation and rehydration of komatiite solutions (Fig. 8) shows that, in general, element concentrations are lower for the tonalite systems.

3.2.5. Temperature effects on solutions resulting from tonalite weathering and evaporation. Values of Mg_T and P_T decreased, whereas Fe_T increased with increasing temperature under all conditions examined in the tonalite weathering and evaporation systems (Supplementary Fig. S5). The behavior of calcium was different, where Ca_T values decreased slightly with temperature under various conditions studied except at $P_{\rm CO2}\!=\!5$ atm in the EE system (Supplementary Fig. S5d). The corresponding results for the komatiite system (Fig. 12) also show consistent trends for $Mg_T,\,P_T,$ and Fe_T with increasing temperature, whereas Ca_T behaved differently.

4. Discussion

This study is the first comprehensive attempt to model the speciation of a large number of elements (14) under Hadean conditions. It is obvious that several assumptions had to be made and ranges of parameters had to be estimated. We first summarize the main results, and then discuss their implications for prebiotic geochemistry in priming the origins of life and the implications of biology for constraining early Earth geochemistry. Next, we address in detail the assumptions made in our modeling approach and the potential effects of these assumptions on model results. Finally, we discuss the importance of the atmospheric redox state.

4.1. Summary of results

In the komatiite system, metal aluminosilicates (i.e., clays), dolomite, gibbsite, pyrite, and HAP were formed at lower P_{CO2} values; magnesite, dolomite, pyrite, and HAP

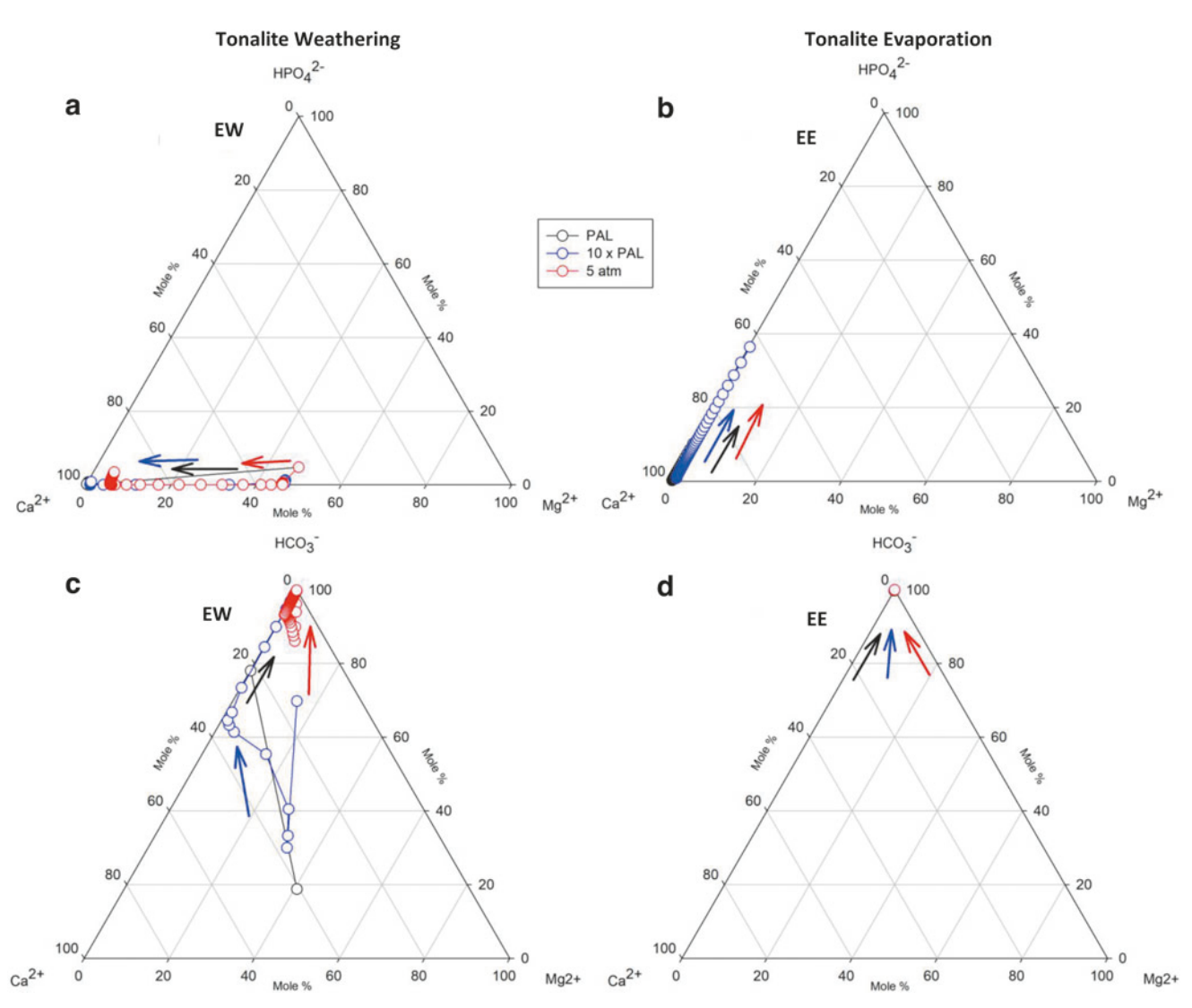


FIG. 15. Evolution of solution composition during tonalite weathering (left panel: \mathbf{a} , \mathbf{c}) and evaporation (right panel: \mathbf{b} , \mathbf{d}) reaction paths at 75°C and various P_{CO2} values shown as ternary diagrams. The upper panels show HPO_4^{2-} , Ca^{2+} , and Mg^{2+} concentrations (mole %) at the apices of the ternary plots (\mathbf{a} , \mathbf{b}) and the lower panels show HCO_3^{-} , Ca^{2+} , and Mg^{2+} concentrations (mole %) at the apices of the ternary plots (\mathbf{c} , \mathbf{d}). No geochemical divide is seen between Ca and Mg during either the weathering reaction path (\mathbf{a} , \mathbf{c}) or during the evaporation reaction path (\mathbf{b} , \mathbf{d}) in both phosphate and carbonate ternary diagrams. Starting composition for the evaporation reaction path was the tonalite ($c_{HAP, p} = 1$ g/kg tonalite) EW solution at various values of P_{CO2} and P_{CO2} an

were still formed at higher $P_{\rm CO2}$ values, but metal aluminosilicates were replaced by chalcedony and kaolinite (pure aluminosilicate). HAP was precipitated during weathering but not during evaporation, and so, $P_{\rm T}$ increased with each evaporation-rehydration cycle, while $Mg_{\rm T}$, $Ca_{\rm T}$, and $Fe_{\rm T}$ decreased as other minerals precipitated out.

In general, for all $P_{\rm CO2}$ values, the concentrations of ${\rm Mg}^{2+}$ and ${\rm HPO_4}^{2-}$ became lower and the ${\rm HCO_3}^-$ concentration increased as the temperature increased, consistent with retrograde solubility of the minerals controlling those ions' concentrations. Pyrite has prograde solubility, and so, the concentration of ${\rm Fe}^{2+}$ increased with temperature. Similarly, the concentration of ${\rm Ca}^{2+}$ increased with temperature in systems where huntite was formed at 25°C, but this phase was replaced by dolomite at higher temperatures.

Weathering of tonalite with increasing $P_{\rm CO2}$ values and evaporation of the solution produced a change in the suite of minerals and solution concentration trends with temperature similar to those observed for komatiite weathering.

We discuss below the implications of the solution compositions for prebiotic RNA formation and protocell self-assembly.

4.2. Implications of results for prebiotic chemistry and carbon cycling

4.2.1. Komatiite solutions. It has been proposed that, prebiotically, Fe^{2+} may have played the role that Mg^{2+} plays in many biochemical reactions based on the observation that Fe^{2+} is a much more efficient catalyst than Mg^{2+} in some model prebiotic chemistry experimental studies (Hsiao

et al., 2013; Bray et al., 2018; Jin et al., 2018a). We examine here whether the divalent cation concentrations and P_T concentrations obtained from komatiite weathering reactions are consistent with these proposals and with model fatty acid protocell membrane stability.

At 25°C, biological levels of magnesium (millimolar) and ferrous iron (10s of micromolar) were obtained at $P_{CO2}=5$ atm in komatiite EW solutions (Figs. 10 and 11). At $P_{CO2} = 5$ atm and T = 25°C, our regression analysis suggests that $P_T = 1$ molal is achieved after 175 cycles (Fig S2; Supplementary Table S2). At this number of cycles, our regressions suggest that Mg_T=0.18 molal, while Ca_T and Fe_T are below nanomolar levels (Fig. S1 and Supplementary Table S2). This high value of Mg_T is not compatible with fatty acid-based protocell membrane self-assembly. Furthermore, the estimated nanomolar concentrations for Fe_T are probably too low to promote RNA template-directed polymerization, which requires $\sim 80 \,\mathrm{mM}$ Fe_T (Jin et al., 2018a); or to support the role of Fe²⁺ as a cofactor for ribsomal RNA-promoted single electron transfer reactions, which functions at micromolar levels (Hsiao et al., 2013); or to permit Fe²⁺-promoted bacterial translation, which occurs at millimolar levels of Fe²⁺ (Bray et al., 2018).

At 75° C, biologically relevant levels were achieved at $P_{CO2}=1$ atm for magnesium (millimolar) and ferrous iron (micromolar) in komatiite EW solutions (Figs. 3 and 4 and Table 2 Section A); millimolar P_{T} and micromolar to tens of micromolar Fe^{2+} were obtained at $P_{CO2} \ge 5$ atm in EE solutions after one cycle of evaporation (Figs. 3 and 5 and Table 2 Section B). The Fe^{2+} concentrations we obtained are consistent with a previous estimate of ~ 0.1 mM for Precambrian oceans (Halevy *et al.*, 2017), but lower than that of Hao *et al.* (2017), who suggested 0.1 mM in Archean riverwater.

To summarize, the present study shows that the Fe^{2+} concentration would have been orders of magnitude less than that of Mg^{2+} . This result suggests that prebiotic chemistry experiments that contain much lower levels of Fe^{2+} would provide a more robust test of the hypothesis that Fe^{2+} is more efficient than Mg^{2+} as a catalyst and that Fe^{2+} may have been the initial cocatalyst that was eventually replaced by Mg^{2+} .

We next consider "the phosphate problem." Considering prebiotic RNA formation and protocell survival, at $P_{\rm CO2}=5$ atm and $T=75^{\circ}{\rm C}$, a $P_{\rm T}=1$ molal required for the Powner et al. (2009) synthesis of RNA mononucleotides would be achieved after 555 rehydration/evaporation cycles (Supplementary Table S2). This phosphate concentration would promote nonenzymatic RNA mononucleotide synthesis by the Powner et al. (2009) synthesis route. Interestingly, after this number of cycles, the divalent cation concentrations would simultaneously be low enough to allow fatty acid membrane self-assembly to form a protocell (Mg_T \sim 0.4 µmolal, Ca_T \sim 8 nmolal, and Fe_T \sim 0.5 nmolal).

While these low Mg_T and Fe_T values are not high enough to support template-directed nonenzymatic RNA polymerization, montmorillonite-catalyzed RNA polymerization is still possible even in the total absence of magnesium (Kaddour *et al.*, 2018), especially when cocatalysts, such as acidic α -amino acids or neutral nonpolar α -amino acids, are also present (Namani *et al.*, 2021). With a stable protocell membrane, transmembrane gradients of K^+/Na^+ could be generated across mixed fatty acid-phospholipid membranes

(Zhou *et al.*, 2020). Likewise, transmembrane H⁺ gradients coupled with NAD⁺ to NADH reduction could be achieved by photocatalytic minerals in the environment to support metabolism (Dalai and Sahai, 2019b).

At first glance, the 555 rehydration/evaporation cycles appear to be a very long time to be plausible for promoting prebiotic RNA monomer synthesis (i.e., to achieve $P_T = 1 M$). However, recall that during the Hadean, each day lasted only \sim 6 h (one-quarter of modern Earth day). Assuming that each wet/dry cycle corresponds to one diurnal cycle, 555 rehydration/ evaporation cycles would correspond to only ~ 139 day/night cycles on modern Earth. Furthermore, the Moon was much closer to the Earth, and so, the tidal ranges would have been huge and would have affected even lake shores substantially, thus allowing two more wetting-drying cycles within each day. Thus, 555 rehydration/evaporation cycles could have been achieved in only ~ 70 days on modern Earth. Thus, nucleotide synthesis by Powner et al.'s (2009) approach would be plausible at $T \sim 75$ °C and $P_{CO2} \sim 5$ atm. Furthermore, this abundant concentration of P_T would facilitate the formation of imidazole phosphate, which further promotes phosphorylation of a wide range of biologically relevant organic molecules (Maguire et al., 2021).

It is important to note that other completely different approaches have been taken to address the "phosphate problem," which rely on reactions of reduced phosphorus species (Pasek, 2008; Pasek *et al.*, 2013, 2014, 2017; Ritson *et al.*, 2020). Schreibersite [(Fe₃Ni)P], a mineral formed by meteoritic impacts and lightning, has been proposed as a source of phosphite on early Earth. Phosphite has been identified in trace quantities in Archean rocks and on modern Earth (Pasek, 2008; Pasek *et al.*, 2013, 2014, 2017). This phosphite would subsequently have to be oxidized to phosphate to be made bioavailable. It has been shown that phosphite (PO₃) derived from the oxidative dissolution of schreibersite is capable of phosphorylating adenosine to form adenosine monophosphate (Gull *et al.*, 2015).

Furthermore, reduced phosphorus species, which may be released by weathering of schreibersite [(Fe, Ni)P₃], yield phosphate when irradiated by ultraviolet light in the presence of H₂S/HS⁻ (Ritson *et al.*, 2020). The extent to which this reaction could proceed depends on H₂S/HS⁻ concentration (50 μ M HS⁻ was used by Ritson *et al.*, 2020) remains to be explored and also whether this concentration was achievable on early Earth. In particular, at a plausible P_{H₂S} of 1×10^{-6} atm, HS⁻ concentration is estimated to be $\leq 1 \mu$ M (Ranjan *et al.*, 2018). This could be tested easily in future experiments using lower HS⁻ concentrations than have been used to date in model prebiotic chemistry experiments.

4.2.2. Tonalite solutions. Tonalite weathering and one cycle of evaporation did not result in concentrations of any relevant ions for prebiotic chemistry aspects considered here, such as RNA monomer synthesis, RNA template-mediated polymerization or fatty acid membrane self-assembly (Fig. 14, Table 3, and Supplementary Table S5). The biological level of P_T was obtained at 75°C and P_{CO2} =5 atm, and high levels of magnesium (0.1–0.01 molal) were observed at 25°C and P_{CO2} =5 atm (Supplementary Table S5). Solution compositions that can promote ribonucleotide synthesis would require tens of thousands or an even greater number of dehydration-rehydration cycles

(Supplementary Table S3). Hence, solutions produced by weathering of tonalite and followed by evaporation are deemed as not enabling prebiotic chemistry.

4.2.3. Carbon cycling. The deposition of large quantities of sedimentary carbonate rocks is an outcome of the komatiite weathering and solution evaporation processes described above. The observed paucity of carbonates in Archean rocks might reflect a preservation bias, where the carbonates and oceanic crust were recycled to produce carbonatites by ~ 3.0 Ga (Bizzarro *et al.*, 2002; Rukhlov and Bell, 2010) and, potentially, as early as ~ 4.26 Ga (Hoernle *et al.*, 2002; Sleep, 2010; Hazen *et al.*, 2013). Subducted carbonates might also be stored as deep carbon diamonds and supercritical fluids in the lower mantle (Walter *et al.*, 2011; Sverjensky *et al.*, 2014; Keleman and Manning, 2015).

4.2.4. Trace element abundance. The mafic to ultramafic rock composition (komatiite) is found to be more favorable for many of the major elements (C, Mg, Ca, Fe, P,) required for favorable prebiotic chemistry, whereas the intermediate rock composition (tonalite) is not as promising a candidate. One important outcome of this result is that the corresponding trace elements that would be associated with komatiite are elements, such as Co, Ni, Cr, Cu, Ru and V, would be more likely to occur, versus Zn, Mo and W, that would be more enriched in tonalite or granodioritic compositions. A caveat, however, is that the actual availability of all these trace elements would likely be highly limited by the very insoluble nature of their corresponding sulfide minerals, similar to the behavior of Fe²⁺ as constrained by pyrite, that we have observed here.

4.3. Significance of the modeling approach

4.3.1. Comprehensive and quantitative speciation approach. It is important to underscore the significance of the comprehensive geochemical modeling approach taken here. Consideration of the simultaneous equilibrium speciation of multiple elements in various phases yields quantitative ion concentrations of all 14 elements included, and provides the secondary minerals formed. The element concentration ranges, speciation, and pH values obtained from subaerial weathering of komatiite provide some constraints for organic chemists to design nonenzymatic synthesis experiments modeling prebiotic processes. For example, the precipitation of saponites (Mg-enriched clay) during 75°C weathering and evaporation of both komatiite and tonalite at lower values of P_{CO2} but not at higher P_{CO2} values is important in controlling Mg²⁺ concentration in solution, along with the formation of magnesite and dolomite. Saponite is commonly found in evaporitic lake environments along with carbonates as a result of direct precipitation from solution (Jones and Conko, 2011), so its predicted formation is a reasonable outcome of the present model at low P_{CO2} values. These considerations also support the robustness of the present reaction path modeling approach and of the accuracy of the Thermo database modified for the solubility product of HAP (Sahai and Schoonen, 2020) (see Methods in Section 2.0). Such delicate controls on solution behavior (ion concentrations and speciation) as well as the formation of specific secondary minerals at low versus high values of P_{CO2} influence the geochemical divide and whether phosphate remains in solution or not, and are not accounted for by box modeling approaches (e.g., Toner and Catling, 2020).

4.3.2. Universal geological processes. Significantly, we showed that *common* geological processes of weathering and evaporation produced solutions favorable for the synthesis and self-assembly of some of the fundamental molecular building blocks of a protocell. Thus, special *ad hoc* local geochemical scenarios did not need to be invoked. This point is addressed further in Section 4.4. Also, these geological processes acted on the *oldest* crustal rocks (komatiite) suggesting that protocells could have evolved very early in Earth history.

4.3.3. Prebiotic chemistry on other worlds. Primary rocks on other solid worlds, such as Mars, Moon, Io, Ganymede, Enceladus, and perhaps, even exo-solar planets (Spiegel *et al.*, 2014), are composed of silicates similar to certain modern basalts. These bodies could, potentially, have had komatiite-like precursors in their early history; even tonalite might exist on Mars (Sautter *et al.*, 2015). Thus, the modeling approach taken here could be applied to such other worlds with appropriate atmospheric chemistry, and if liquid water existed, to determine the availability and speciation of important elements for prebiotic nucleotide synthesis and polymerization, as well as for protocell membrane self-assembly.

4.4. Biological implications for geochemistry

While geochemical constraints provided plausible ranges of ion availability for biological and prebiotic syntheses, conversely, the biological and prebiotic synthesis requirements helped to narrow the range of early Earth geochemical conditions, in particular, $P_{\rm CO2}$. Optimal $P_{\rm T}$, $Mg_{\rm T}$, $Ca_{\rm T}$ and $Fe_{\rm T}$ concentrations were obtained at $P_{\rm CO2} \sim 1-5$ atm. This range of $P_{\rm CO2}$ is consistent with previous independent $P_{\rm CO2}$ estimates for Hadean Earth that place the limits at 0.2–10 atm (Walker, 1985; Kasting, 1993).

One of the most important results of the present work is that prebiotic synthesis could occur even under neutral atmospheric conditions with average global freshwater or evaporite brine compositions. This does not preclude the possibility that there were local environments with conditions very different from the average solution chemistries considered here. Those local conditions could also have promoted prebiotic RNA synthesis and protocell membrane assembly. The important point is that the present results show that those special local environments may be sufficient but are not necessary, and prebiotic synthesis could have occurred anywhere on a komatiitic surface with wetting-drying cycles under the appropriate conditions of $P_{\rm CO2}$, $P_{\rm H2S}$ and temperature.

4.5. Influence of model assumptions on results

4.5.1. Source of phosphate. HAP is the dominant form of apatite in ultramafic and mafic rocks such as komatiite, although apatite usually occurs as a solid solution of fluorand hydroxyl-forms. The fluor-forms being more common in granitic or granodioritic rocks and the hydroxyl-forms being more common in komatiites. Fluorapatite is many orders of magnitude less soluble than HAP, and so, much less phosphorus would be released during weathering of tonalitic or granodioritic rocks comprising protocontinental crust. Therefore, our calculations using HAP represent a high endmember scenario, which is appropriate for komatiite.

4.5.2. Redox states. The redox state of various elements (C, N, P, S, and Fe) has to be considered under Hadean

Earth conditions. The oxidation state of the early atmosphere is a topic of active research and depends on the assumed source of the gases (Zahnle *et al.*, 2010; Catling and Kasting, 2017). If it is assumed that early Earth composition was similar to ordinary H-type chondrites, then the formation of the early atmosphere by impact degassing of such a rock type results in a relatively neutral atmosphere, with N₂, CO₂, and H₂O as the dominant gases. In contrast, impact degassing of an early Earth composition similar to CI-type carbonaceous chondrites results in CH₄, H₂, and CO as the dominant gases. This is an open question, but many geochemists accept that the early Earth was more similar to ordinary H-type chondrites (Catling and Kasting, 2017), which is assumed here.

We assumed that CO₂ did not undergo redox reactions, because its abiotic reduction to CH₄ is extremely slow at Earth's surface conditions (Schoonen *et al.*, 2004). If we had assumed the alternative reducing atmosphere, then the abundance of phosphate would be lower than predicted in our models, and other phosphorylation reactions, such as those involving a urea/ammonium formate/water eutectic (Burcar *et al.*, 2016, 2019), would become more plausible.

The effects of sulfur redox state was examined by sensitivity analysis of changing P_{H2S} and SO_4^{2-} concentrations. It was found that P_T , Mg_T and Ca_T changed slightly, whereas Fe_T increased because less pyrite precipitated as P_{H2S} decreased and aqueous SO_4^{2-} concentrations decreased for komatiite EW and EE solutions at $P_{CO2} = 5$ atm and $T = 75^{\circ}C$.

The oxidation of Fe(II) to Fe(III) is not considered in the present study. Some oxidation of Fe(II) to Fe(III) would have occurred on Hadean Earth by Fenton-type reactions due to photolytic splitting of water or by reaction with SO_4^{2-} . Because ferric oxyhydroxides would have been transient species in the absence of atmospheric O_2 , there are very poor limits on their available concentrations. The small amount of iron oxyhydroxides produced by such reactions could have adsorbed dissolved phosphate, but the ferric oxyhydroxides would be highly reactive under a non-oxygenic atmosphere and would rapidly redissolve, thus releasing the adsorbed phosphate. Therefore, the effect of the Fe(II)/Fe(III) redox couple is expected to be negligible for the present considerations.

Phosphorous exists almost entirely in the +5 oxidation state down to very low oxygen fugacities, that is, extremely reducing conditions (Pasek and Kee, 2011; Pasek et al., 2014). Hence, we did not consider reduced P species. For the phosphate minerals, HAP and whitlockite are present in the Thermo thermodynamic database and were included in the models. Strengite (FePO₄.2H₂O), berlinite (AlPO₄), vivianite [(Fe₃(PO₄)₂. 8H₂O], and struvite (NH₄MgPO₄.6-H₂O) are not part of the Thermo database. Equilibrium constants from other sources for these minerals were not included for the following reasons. Strengite contains Fe(III) iron, which is not considered significant in the present study, as discussed above. Berlinite is a very rare mineral and is only found in high-temperature hydrothermal deposits, and so, it is outside the stability range of the 75°C conditions considered here.

Vivianite contains Fe(II), but it is not included for two reasons. First, because HAP is the primary source of P in the weathering reactions (vivianite does not occur in komatiite or tonalite); and second, vivianite is not included in the evaporation step because weathering neutralizes the solution

pH to \sim 5-6 by the end of the 5% komatiite or tonalite weathering reaction at $P_{\rm CO2} \ge 0.5$ atm. At this pH range, vivianite is not expected to control phosphate solubility. Struvite is not considered because we do not include NH₃ speciation in our model, which assumes a neutral atmosphere for early Earth and struvite is a very soluble mineral under such conditions.

Finally, it is well known in the geochemical modeling field, that including thermodynamic equilibrium constants from different sources in the literature is fraught with problems, as values can vary widely for the same mineral and this can produce spurious results (*e.g.*, May and Murray, 2001; Sahai and Schoonen, 2020). The advantage of limiting the calculations to the phosphate minerals contained in the Thermo database is that it is considered the gold standard for internal consistency (Wolery, 1992a, 1992b).

4.5.3. Metal-organic complexation and ion adsorption reactions. The present approach does not account for complexation reactions of metal ions with prebiotic organic molecules in the environment, nor does it account for adsorption of cations and anions on mineral surfaces (i.e., surface complexation). Both these processes would decrease the free ion availability to lower values than predicted by the present model. Inclusion of these reactions would be ideal. Thermodynamic data (complexation constants and adsorption constants, and enthalpies of these reactions) are available for some ions, organic molecules and mineral surfaces, which are internally consistent with the Thermo database (e.g., Shock and Koretsky, 1993, 1995; Sverjensky and Sahai, 1996, 1998; Sahai and Sverjensky, 1997a, 1997b; Koretsky et al., 1998; Sahai, 1998; Prapaipong et al., 1999; LaRowe and Helgeson, 2006). However, some serious challenges exist to taking such an approach. For example, the total concentration of each available organic molecule would need to be known a priori. Similarly, the reactivespecific surface areas and surface site densities of various minerals would need to be known and this information is available for only a handful of minerals. Thus, developing a practical and realistic approach for inclusion of metal/ organic complexation in solution and surface complexation could be considered in a future study.

4.5.4. Wet-dry cycling. The present study assumes 95% evaporation for each evaporative cycle. A caveat is that at high temperatures, such as 75°C, the pressure of water vapor ($P_{\rm H2O}$) could also be correspondingly high and evaporation may not have proceeded to 95% completion on a regular basis. Furthermore, in estimating the number of Hadean diurnal cycles to achieve $P_{\rm T}$ =1 M (Section 4.2.1), it is assumed that each rehydration-evaporation cycle corresponds to a six-hour diurnal cycle. Of course, this need not have occurred with every diurnal cycle, and so, the ~70-day estimate to reach $P_{\rm T}$ =1 M is a rough estimate of the best-case scenario.

The broader point, however, is that high enough values of P_T can be achieved by wetting-drying cycles at "reasonably" high T (75°C) and P_{CO2} (5 atm) values based on geochemical evidence (see Section 2) in a reasonable time period (corresponding to months on modern Earth) compared with geological timescales. Moreover, these cyclically evaporative brines resulted in low divalent cation

concentrations, compatible with protocell membrane stability and with amino acid-promoted montmorillonite-catalyzed RNA polymerization (Namani *et al.*, 2021). However, the divalent cation concentrations in such cyclically evaporative brines at $T=75^{\circ}C$ and $P_{CO2}=5$ atm are too low to promote template-directed nonenzymatic RNA polymerization. Mg^{2+} concentrations high enough to promote RNA template-directed nonenzymatic RNA polymerization are found in the solutions produced by weathering komatiite at $T=75^{\circ}C$ and $P_{CO2}=5$ atm.

4.6. Atmospheric redox state

4.6.1. Phosphorylation under reducing atmosphere conditions. The challenges of prebiotic mononucleotide synthesis and phosphorylation under a neutral atmosphere are significantly removed, if a reducing atmosphere is assumed. Under such conditions, ammonia, methane and H₂ would be stable gases. Dissolved phosphate anion or various phosphate minerals in the presence of urea/ammonium formate/ water eutectic can also phosphorylate adenosine (Burcar *et al.*, 2016, 2019). The ultimate goal is to achieve adenosine triphosphate, which is the activated form, although this is yet to be attained (Pasek *et al.*, 2017).

These are excellent approaches, but it is not known whether the concentrations of urea and ammonium formate required for this eutectic (Burcar *et al.*, 2016, 2019) are prebiotically plausible under a neutral atmosphere. This problem could potentially be overcome in a reducing atmosphere, but a comprehensive modeling approach in which the stability of a large number of elements along with komatiite, the dominant primary rock on early Earth, under reducing atmospheric conditions has not been attempted to date. This comprehensive approach is critical because we have seen that the presence of other cations (*e.g.*, Na⁺ and K⁺) and anions (silicate and bicarbonate) as well as the partial pressure of atmospheric gases can significantly affect which minerals are stable and thus the concentrations of available dissolved species.

A partial approach has been taken in which a system consisting of NH₃, CO₂, phosphate, Mg, Ca, and Fe has been examined under a range of redox potentials (E_h) to estimate the stability of phosphate minerals (Burcar *et al.* 2019). Under those conditions, vivianite and struvite are predicted to be stable. However, the values of NH₃ and CO₂ were obtained for very specific conditions (decomposition of a 10 mM urea solution) and P_T was set at 1 mM; also, the effect of sulfide, which could combine with Fe²⁺ to form pyrite, was not considered. Hence, it is not clear whether the results of that study can be considered sufficiently general to represent early Earth conditions.

In a different approach, diamidophosphate has been shown to phosphorylate a wide range of compounds resulting in the formation of nucleotides and short nucleotide oligomers (tetramers) (Krishnamurthy *et al.*, 1999; Gibard *et al.*, 2017). However, diamidophosphate itself requires cyclic trimetaphosphate for its synthesis and the prebiotic availability of cyclic trimetaphosphate is generally considered implausible; recent efforts have been made to address this issue (Gibard *et al.*, 2019; Maguire *et al.*, 2021).

4.6.2. Alternating neutral and reduced atmospheres. The long-standing debate on whether the early

Earth had a neutral or reducing atmosphere may be closer to being resolved in the light of recent studies. This would have implications for conditions prevalent during prebiotic synthesis of the building blocks of life. For example, four of the five biologically utilized nucleobases have been generated in experiments simulating high-velocity impacts (Ferus et al., 2014). Theoretical models have shown that a Venuslike, neutral atmosphere could persist for long periods of time and then be reduced by a large FeNi-rich bolide impact that would, however, last for only $\sim 1-10$ million years before dissipating back to a neutral atmosphere (Benner et al., 2019; Sossi et al., 2020; Zahnle et al., 2020). Organic synthesis could proceed relatively easily under such reduced atmospheric conditions. However, one of the most significant outcomes of the present results is that they allow us to propose that prebiotic synthesis could occur even under neutral atmospheric conditions within the framework of a single unified mechanism of average global atmospherewater-rock interactions without invoking specialized local environments.

5. Conclusions

The availability of dissolved inorganic phosphate, magnesium, calcium, iron, carbonate and sulfide in geochemical environments is orders of magnitude different from the concentrations required for nonenzymatic prebiotic synthesis, polymerization, and self-assembly of the molecular building blocks of life, namely, nucleotides, adenosine phosphates, and phospholipids. Using a thermodynamic modeling approach, we showed here that atmosphere-waterrock interactions under partial pressures of atmospheric CO₂ (P_{CO2}) and temperatures plausible on early Earth provide realistic constraints on concentrations and speciation of 14 elements simultaneously. The delicate balance of ion concentrations and speciation as well as suites of coexisting secondary minerals formed by weathering of rocks, evaporation of the resulting end-of-weathering solutions, and wetting-drying cycles cannot be accounted for by box modeling approaches.

These results can guide future prebiotic synthesis experiments. In particular, weathering of komatiite and dehydration-rehydration cycles of the solution at $P_{\rm CO2} \sim 1-5$ atm and 75°C produced conditions compatible with prebiotic RNA synthesis, polymerization, and protocell membrane stability. Conversely, the biologically required ion concentrations constrained $P_{\rm CO2}$ on early Earth. Our study provides a single mechanism to quantitatively define solution compositions and $P_{\rm CO2}$, thus providing a palimpsest for abiogenesis.

The present results provide solution composition ranges under neutral atmospheric conditions on early Earth, that would have lasted for a long period of time and could have alternated with brief periods of reducing atmospheres produced by large FeNi-rich bolide impacts. We show that prebiotic nucleotide synthesis, RNA polymerization and protocell membrane self-assembly could occur even under neutral atmospheric conditions with average global freshwater and evaporite brine solution compositions, thus supporting a facile origins-of-life hypothesis. Indeed, the same conclusion has been reached with the discovery of bacterial microfossils in banded iron formations dated to 4.28 to 3.75 Ga in the Nuvvuagittuq Supracrustal Belt, Canada (Papineau *et al.*, 2022),

suggesting that life got a very early start on Earth and within a very short time-span. Special local environments that could promote prebiotic RNA synthesis and protocell self-assembly most likely existed and contributed to the total organic inventory. Thus, local microenvironments were sufficient but not necessary, and prebiotic montmorillonite-catalyzed RNA polymerization and protocell self-assembly could have occurred anywhere on a komatiite surface subjected to weathering and wetting-drying cycles under appropriate conditions temperature and atmospheric composition.

In summary, the present approach brings together the geochemical, biochemical, and organic synthesis fields in the origins of life field. Furthermore, there has been much recent progress in the Origins of Life and Astrobiology field on prebiotic organic synthesis under wetting-drying conditions, which makes the present work even more pertinent because it also provides the experimentalists a basis for setting average global solution chemistry. Finally, the methods we have developed also provide the basis for future work to model solution chemistry on other planets such as Mars, Venus or on other rocky bodies.

Acknowledgment

We are particularly grateful to one of the reviewers for a detailed and highly constructive review that helped improve the presentation of the results.

Author Disclosure Statement

No competing financial interests exist.

Funding Information

Financial support was provided to N.S. by NASA 80NSSC18K1139 subaward RK558-G2, NSF EAR grant number EAR-1829695, Simons Foundation grant number 290359, generous private gifts from Dr. Edward Weil and start-up funds from the University of Akron. M.A.S., Brookhaven National Laboratory, is supported by the DOE-Office of Science.

Supplementary Material

Supplementary Figure S1

Supplementary Figure S2

Supplementary Figure S3

Supplementary Figure S4

Supplementary Figure S5

Supplementary Table S1

Supplementary Table S2

Supplementary Table S3

Supplementary Table S4

Supplementary Table S5

References

- Adamala K and Szostak JW (2013) Nonenzymatic templatedirected RNA synthesis inside model protocells. *Science* 342: 1098–1100.
- Bedoin L, Alves S, and Lambert J-F (2020) Origins of life and molecular information: selectivity in mineral surface induced prebiotic amino acid polymerization. *ACS Eart Space Chem* 4:1802–1812.

Belmonte L and Mansy SS (2016) Metal catalysts and the origin of life. *Elements* 12:413–418.

- Benner SA, Bell EA, Biondi E, et al. (2019) When did life likely emerge on Earth in an RNA-first process? Chem Syst Chem 1:e900035.
- Bethke CM (2008) Geochemical and Biogeochemical Reaction Modeling. Cambridge University Press, New York.
- Bizzarro M, Simonetti A, Stevenson RK *et al.* (2002) Hf isotope evidence for a hidden mantle reservoir. *Geology* 30:771–774.
- Bray MS, Lenz TK, Haynes JW, *et al.* (2018) Multiple prebiotic metals mediate translation. *Proc Natl Acad Sci U S A* 115: 12164–12169.
- Brown PM and Silvius JR (1989) Stability and fusion of lipid vesicles containing headgroup-modified analogues of phosphatidylethanolamine. *Biochim Biophys Acta* 980:181–190.
- Burcar B, Castaneda A, Lago J, *et al.* (2019) A stark contrast to modern Earth: phosphate mineral transformation and nucleoside phosphorylation in an iron- and cyanid-rich early Earth scenario. *Angew Chem Int Ed* 58:16981–16987.
- Burcar B, Pasek M, Gull M, *et al.* (2016) Darwin's warm little pond: a one-pot reaction for prebiotic phosphorylation and the mobilization of phosphate from minerals in a urea-based solvent. *Angew Chem Int End* 55:1–6.
- Burnham AD and Berry AJ (2017) Formation of Hadean granites by melting of igneous crust. *Nat Geosci* 10:457–461.
- Catling DC and Kasting JF (2017) Atmospheric Evolution on Inhabited and Lifeless Worlds. Cambridge University Press, Cambridge, U.K., pp 182, 189.
- Cawood PA, Hawkesworth CJ, and Dhuime B (2012) The continental record and the generation of the continental crust. *GSA Bull* 125:14–32.
- Cleaves HJ, III, Scott AM, Hill FC, et al. (2012) Mineralorganic interfacial processes: potential roles in the origin of life. Chem Soc Rev 41:5365–5568.
- Dalai P and Sahai N (2019a) Mineral-lipid interactions in the origins of life. *Trends Biochem Sc* 44:331–341.
- Dalai P and Sahai N (2019b) Protocell emergence and evolution. In *Handbook of Astrobiology*, edited by V. Kolb, CRC Press, Boca Raton, FL, Chapter 7.2., pp. 491–517.
- Dalai P and Sahai N (2019c) A model photoheterotrophic protometabolism across protocell membranes promoted by photocatalytic minerals. *J Phys Chem C* 124:1469–1477.
- Dalai P, Kaddour H, and Sahai N (2016) Incubating life: prebiotic sources of organics for the origins of life. *Elements* 12: 401–406.
- Dalai P, Ustriyana P, and Sahai N (2018) Aqueous magnesium as an environmental selection pressure in the evolution of phospholipid membranes on early Earth. *Geochim Cosmochim Acta* 223:216–228.
- Damer B and Deamer D (2015) Coupled phases and combinatorial selection in fluctuating hydrothermal pools: a scenario to guide experimental approaches to the origin of cellular life. *Life* 5:872–887.
- Deamer DW and Pashley RM (1989) Amphiphilic components of the Murchison carbonaceous chondrite—surface-properties and membrane formation. *Orig Life Evol Biosph* 19:21–38.
- Dzombak DA and Morel FMM (1990) Surface Complexation Modeling: Hydrous Ferric Oxide. Wiley, New York, NY, p. 416.
- Ferris JP and Ertem G (1992) Oligomerization of ribonucleotides on montmorillonite: reaction of the 5'-phosphorimidazolide of adenosine. *Science* 257:1387–1389.

- Ferus M, Nesvorny D, Sponer J, *et al.* (2014) High-energy chemistry of formamide: a unified mechansm of nucleobase formation. *Proc Natl Acad Sci U S A* 112:657–662.
- Forsythe JG, Yu S-S, Mamajanov I, *et al.* (2015) Estermediated amide bond formation driven by wet-dry cycles: a possible path to polypeptides on the Prebiotic Earth. *Angew Chem Int Ed* 54:9871–9875.
- Gibard C, Bhowmik S, Karki M, *et al.* (2017) Phosphorylation, oligomerization and self-assembly in water under potential prebiotic conditions. *Nat Chem* 10:212–217.
- Gibard C, Gorrell IB, Jimenez EI, *et al.* (2019) Geochemical sources and availability of amidophosphates on early Earth. *Angew Chem Int Ed* 58:8151–8155.
- Gulick A (1955) Phosphorus as a factor in the origin of life. *Am Sci* 43:479–489.
- Gull M, Mojica MA, Fernandez FM, *et al.* (2015) Nucleoside phosphorylation by the mineral schreibersite. *Sci Rep* 5: 17198.
- Halevy I, Alesker M, Schuster EM, et al. (2017) A key role for green rust in the Precambrian oceans and the genesis of iron formations. Nat Geosci 10:135–139.
- Hanczyc MM, Fujikawa SM, and Szostak JW (2003) Experimental models of primitive cellular compartments: encapsulation, growth, and division. *Science* 302:618–622.
- Hao J, Sverjensky DA, and Hazen RM (2017) A model for late Archean chemical weathering and world average river water. *Earth Planet Sci Lett* 457:191–203.
- Hardie LA (1987) Dolomitization: a critical view of some current views. *J Sediment Res* 57:166–183.
- Hardie LA and Eugster HP (1970) The evolution of closed-basin brines. *Mineral Soc Am Spec Paper* 3:273–290.
- Hazen RM, Downs RT, Kah L, et al. (2013) Carbonate mineral evolution. In Carbon in Earth, Reviews in Mineralogy and Geochemistry Series, Vol. 75, Mineralogical Society of American, Washington, D.C., pp 79–107.
- Hoernle K, Tilton G, Le Bas MJ, et al. (2002) Geochemistry of oceanic carbonatites compared with continental carbonatites: mantle recycling of oceanic crustal carbonate. Contrib Mineral Petrol 142:520–542.
- Holland HD (1984) The chemical evolution of the atmosphere and oceans. In *Treatise on Geochemistry*, Vol. 6, edited by H. Elderfield, Elsevier, Oxford, pp 583–625.
- Holland HD (2004) The geologic history of seawater. *Treatise Geochem* 6:583–625.
- Hsiao C, Chou, I-C, Okafor D, *et al.* (2013) RNA with iron (II) as a cofactor catalyses electron transfer. *Nat Chem* 5:525–528.
- Iizuka T, Horie K, Komiya T, et al. (1996) 4.2 Ga zircon xenocryst in an Acasta gneiss from northwestern Canada: evidence for early continental crust. Geology 34:245–248.
- Jackson AM and Jellinek MG (2015) Connections between the bulk composition, geodynamics and habitability of Earth. *Nat Geosci* 8:587–593.
- Jin L, Englehart AE, Zhang W, et al. (2018a) Catalysis of template-directed nonenzymatic RNA copying by Iron (II). J Am Chem Soc 140:15016–15021.
- Jin L, Kamat NP, Jena S, et al. (2018b) Fatty acid/phospholipid blended membranes: a potential intermediate state in protocellular evolution. Small 14:1704077.
- Johnston DT (2011) Sulfur isotopes and the evolution of Earth's surface sulfur cycle. *Earth Sci Rev* 106:161–183.
- Jones BF and Conko KM (2011) Environmental influences on the occurrences of sepiolite and palygorskite: a brief review. In *Developments in Clay Science*, Vol. 3, Chapter 3, edited by E. Galan and A. Singer, Elsevier, pp 69–83.

- Kaddour H, Gerisioglu S, Dalai P, et al. (2018) Non-enzymatic polymerization at the mineral-water interface: an insight into adsorption-polymerization relationships and the effects of magnesium. J Phys Chem C 122:29386–29397.
- Karki M, Gibard C, Bhowmik S, and Krishnamurthy R (2017) Nitrogenous derivatives of phosphorus and the origins of life: Plausible prebiotic phosphrylating agents in water. *Life* 7:32.
- Kasting J (1993) Earth's early atmosphere. *Science* 259:920–926.
- Keleman PB and Manning CE (2015) Revaluating carbon fluxes in subduction zones, what goes down mostly comes up. *Proc Natl Acad Sci U S A* 112:E3997–E4006.
- Koretsky CM, Sverjensky DA, and Sahai N (1998) Calculating site densities of oxides and silicates from crystal structures. *Amer J Sci* 298:349–38.
- Krishnamurthy R, Arrhenius G, and Eschenmoser A (1999) Formation of glycolaldehyde phosphate from glycolaldehyde in aqueous solution. *Orig Life Evol Biosph* 29:333–354.
- LaRowe DE and Helgeson HC (2006) Biomolecules in hydrothermal systems: calculation of the standard molal thermodynamic properties of nucleic-acid bases, nucleosides, and nucleotides at elevated temperatures and pressures. *Geochim Cosmochim Acta* 70:4680–4724.
- Le Maitre RW, Streckeisen A, Zanettin B, et al. (2002) Igneous Rocks: a classification and glossary of terms. In Recommendations of the International Union of Geological Sciences Subcommission on the Systematics of Igneous Rocks, edited by RW Le Maitre, 2nd ed., Cambridge University Press, Cambridge, UK, p. 236.
- Maguire OR, Smockers IBA, and Huck WTA (2021) A physicochemical orthophosphate cycle via a kinetically stable thermodynamically activated intermediate enables mild prebiotic phosphorylations. *Nat Commun* 12:5517.
- Maurel M-C and Leclerc F (2016) From foundation stones to life: concepts and results. *Elements* 12:407–412.
- May PM and Murray K (2001) Database of chemical reactions designed to achieve thermodynamic consistency automatically. *J Chem Eng Data* 46:1035–1040.
- McCollum TM (1999) Methanogenesis as a potential source of chemical energy for primary biomass production by autotrophic organisms in hydrothermal systems on Europa. *J Geophys Res* 104:30729–30742.
- McCollom TM, Ritter G, and Simoneit BRT (1999) Lipid synthesis under hydrothermal conditions by Fischer-Tropsch-Type reactions. *Orig Life Evol Biosph* 29:153–166.
- Mielke JE (1979) Composition of the Earth's crust and distribution of the elements. In *Review of Research on Modern Problems in Geochemistry*, edited by F.R. Siegel, UNESCO Report, Paris, pp 13–37.
- Milo R and Phillips R (2015) *Cell Biology by the Numbers*. Garland Science, Taylor and Francis Group, New York, NY, p 129.
- Monnard P-A and Deamer D (2002) Influence of ionic inorganic solutes on self-assembly and polymerization processes related to the early forms of life: implications for a prebiotic aqueous medium. *Astrobiology* 2:139–152.
- Namani T, Snyder S, Eagan JE, et al. (2021) Amino acid specific nonenzymatic montmorillonite-promoted RNA polymerization. *Chem Syst Chem* 3:e2000060.
- Papineau D, She Z, Dodd MS, *et al.* (2022) Metabolically diverse primordial microbial communities in Earth's oldest seafloor-hydrothermal jasper. *Sci Adv* 8:eabm2296.

Pasek M and Greenburg R (2012) Acidification of Europa's subsurface ocean as a consequence of oxidant delivery. *Astrobiology* 12:1–9.

- Pasek M and Kee T (2011) On the origin of phosphorylated molecules. In *Origins of Life: The Primal Self-Organization*, Chapter 3, edited by R. Egel, D.-H. Lankenau, and A.Y. Mulkidjanian, Springer-Verlag, Berlin, pp 57–83.
- Pasek M, Gull M, and Herschy B (2017) Phosphorylation on the early Earth. *Chem Geol* 475:149–170.
- Pasek MA (2008) Rethinking early Earth phosphorus geochemistry. Proc Natl Acad Sci U S A 105:853–858.
- Pasek MA, Hernmeijer JP, Buick R, et al. (2013) Evidence for reactive reduced phosphorus species in the early Archean ocean. Proc Natl Acad Sci U S A 110:10089–10094.
- Pasek MA, Sampson JM, and Atlas Z (2014) Redox chemistry in the phosphorus biogeochemical cycle. *Proc Natl Acad Sci U S A* 111:15468–15473.
- Peck WH, Valley JH, Wilde SA, *et al.* (2001) Oxygen isotope ratios and rare earth elements in 3.3 to 4.4 Ga zircons: ion microprobe evidence for high-¹⁸O continental crust and oceans in the Early Archean. *Geochim Cosmochim Acta* 65: 4215–4229.
- Poudyal RR, Cakma FP, Keating CD *et al.* (2018) Physical principles and extant biology reveal roles for RNA-containing membraneless compartments in origins of life chemistry. *Biochemistry* 57:2509–2519.
- Poudyal RR, Guth-Mezler RM, Veenis AJ, *et al.* (2019) Template-directed RNA polymerization and enhanced ribozyme catalysis inside membraneless compartments formed by coacervates. *Nat Commun* 10:1–13.
- Powner MW, Gerland B, and Sutherland JD (2009) Synthesis of activated pyrimidine ribonucleotides in prebiotically plausible conditions. *Nature* 459:239–242.
- Prapaipong P, Shock EL, and Koretsky CM (1999) Metalorganic complexes in geochemical processes: temperature dependence of the standard thermodynamic properties of aqueous complexes between metal cations and dicarboxylate ligands. Geochim Cosmochim Acta 63:2547–2577.
- Prothero DR and Dott RH, Jr. (2002) Evolution of the Earth, 2nd ed. McGraw Hill, New York, p 119.
- Ranjan S, Todd ZR, Sutherladn JD *et al.* (2018) Sulfidic concentrations on early Earth. *Astrobiology* 18:1023–1040.
- Reimink JR, Chacko T, Stern RA *et al.* (2014) Earth's earliest evolved crust generated in an Iceland-like setting. *Nat Geosci* 7:529–533.
- Rickard D (2012) The evolution of the sedimentary sulfur cycle. In *Sulfidic Sediments and Sedimentary Rocks*, edited by D. Rickard. Ch 17, pp. 685–766 in Developments in Sedimentology series, v. 65, 801 p. Series Ed. A.J. Van Loon (Series Ed.), Elsevier, Amsterdam.
- Ritson DJ, Mojzsis SJ, and Sutherland JD (2020) Supply of phosphate to early Earth by photogeochemistry after meteoritic weathering. *Nat Geosci* 13:344–348.
- Romanek CS, Jiménez-López C, Rodriguez Navarro A, *et al.* (2009) Inorganic synthesis of Fe-Ca-Mg carbonates at low temperature. *Geochim Cosmochim Acta* 73:5361–5376.
- Rozel AB, Golabek GJ, Jain C, *et al.* (2017) Continental crust formation on early Earth controlled by intrusive magmatism. *Nature* 545:332–335.
- Rukhlov AS and Bell K (2010) Geochronology of carbonatites from the Canadian and Baltic shields, and the Canadian cordillera: clues to mantle evolution. *Miner Petrol* 98:11–54.
- Sahai N and Sverjensky DA (1997a) Evaluation of internallyconsistent parameters for the triple-layer model by the sys-

- tematic analysis of oxide surface titration data. *Geochim Cosmochim Acta* 61:2801–2826.
- Sahai N and Sverjensky DA (1997b) Solvation and electrostatic model for specific electrolyte adsorption. *Geochim Cosmochim Acta* 61:2827–2848.
- Sahai N and Sverjensky DA (1998) GEOSURF: A computer program for modeling adsorption on mineral surfaces in solution. *Computers Geosci* 24:853–873.
- Sahai N (2000) Estimating adsorption enthalpies and affinity sequences of monovalent electrolyte ions on oxide surfaces in aqueous solution. *Geochim Cosmochim Acta* 64:3629– 3641.
- Sahai N and Schoonen MA (2020) Accuracy of thermodynamics databases for hydroxyapatite dissolution constant. Astrobiology 20:157–160.
- Sahai N, Kaddour H, and Dalai P (2016) The transition from geochemistry to biogeochemistry. *Elements* 12:389–394.
- Sahai N, Kaddour H, Dalai P, et al. (2017) Mineral surface chemistry and nanoparticle-aggregation control membrane self-assembly. Sci Rep 7:43418.
- Sautter V, Toplis MJ, Wiens RC, et al. (2015) In situ evidence for continental crust on early Mars. Nat Geosci 8: 605–609.
- Schoonen M and Smirnov A (2016) Staging life on an early warm "seltzer" ocean. *Elements* 12:395–400.
- Schoonen M, Smirnov A, and Cohn CA (2004) A perspective on the role of minerals in prebiotic synthesis. *Ambio* 33:539– 551.
- Schwartz AW (2006) Phosphorus in prebiotic chemistry. *Philos Trasns R Soc Lond B Biol Sci* 361:1743–1749.
- Shock EL and Koretsky CM (1993) Metal-organic complexes in geochemical processes: Calculation of standard state partial molal thermodynamic properties of aqueous acetate complexes at high pressure and temperatures. *Geochim Cosmochim Acta* 57:4899–4922.
- Shock EL and Koretsky CM (1995) Metal-organic complexes in geochemical processes: Calculation of standard state partial molal thermodynamic properties of aqueous complexes between metal cations and monovalent organic acid ligands at high pressure and temperatures. *Geochim Cosmochim Acta* 57:4899–4922.
- Siegfried F, Kossacki KJ, von Bloh W, *et al.* (2002) Long-term evolution of the global carbon cycle: historic minimum of global surface temperature at present. *Tellus* 54B: 325–343.
- Sleep NH (2010) The Hadean-Archaean environment. In *The Origins of Life*, edited by D. Deamer and J.W. Szostak, *Cold Spring Harbor Lab Perspectives in Biology*, Vol. 2, a002527.
- Sossi PA, Burnham AD, Badro J, *et al.* (2020) Redox state of Earth's magma ocean and its Venus-like early atmosphere. *Sci Adv* 6:eabd1387.
- Spiegel DS, Fortney JJ, and Sotin C (2014) Structure of exoplanets. *Proc Natl Acad Sci U S A* 111:12622–12627.
- Sverjensky DA and Sahai N (1996) Theoretical prediction of single-site surface protonation equilibrium constants for oxides and silicates in water. *Geochim Cosmochim Acta* 60: 773–3797.
- Sverjensky DA and Sahai N (1998) Prediction of surfaceprotonation enthalpies for oxides. *Geochim Cosmochim Acta* 62:3703–3715.
- Sverjensky DA, Stagno V, and Huang F (2014) Important role for organic carbon in subduction-zone fluids in the deep carbon cycle. *Nat Geosci* 7:909–913.

Tosca NJ and McLennan SM (2006) Chemical divides and evaporate assemblages in Mars. *Earth Planet Sci Lett* 241: 21–31.

Walker JCG (1985) Carbon dioxide on the early Earth. *Orig Life* 16:117–127.

Walter MJ, Kohn SC, Araujo D, et al. (2011) Deep mantle cycling of oceanic crust: evidence from diamonds and their mineral inclusions. Science 334:54–57.

Wang X-C, Li X-H, Li W-X, et al. (2007) Ca. 825 Ma komatiitic basalts in South China: first evidence for >1500°C mantle melts by a Rodinian mantle plume. Geology 35:1103–1106.

Wolery TJ (1992a) EQ3/EQ6, a software package for geochemical modeling of aqueous systems, package overview and installation guide (version 7.0). Lawrence Livermore National Laboratory, Livermore, CA. Report UCRL-MA-110662, part 1, 66 p.

Wolery TJ (1992b) EQ3NR, a computer program for geochemical aqueous speciation-solubility calculations—theoretical manual, user's guide, and related documentation (version 7.0). Lawrence Livermore National Laboratory, Livermore, CA. Report UCRL-MA-110662, part 3, 246 p.

Yuen GU and Kvenvolden KA (1973) Monocarboxylic acids in Murray and Murchison carbonaceous meteorites. *Nature* 246: 301–303.

Zahnle K (2006) Earth's earliest atmosphere. *Elements* 2:217–222.

Zahnle K, Schaefer L, and Fegley B (2010) Earth's earliest atmospheres. *Cold Spring Harb Perspect Biol* 2. Ch. 4, a004895.
 Zahnle K, Lupu R, Catling DC, *et al.* (2020) Creation and evolution of impact-generated reduced atmospheres of early

Earth. Planet Sci J 1-21.

Zhou X, Dalai P, and Sahai N (2020) Semipermeable mixed phospholipid-fatty acid membranes exhibit K⁺/Na⁺ selectivity in the absence of proteins. *Life* 10. DOI: 10.3390/ life10040039.

Address correspondence to:
Nita Sahai
School of Polymer Science and Polymer Engineering
University of Akron
Akron, OH 44325
USA

E-mail: sahai@uakron.edu

Submitted 19 October 2020 Accepted 28 December 2021 Associate Editor: Norman Sleep

Abbreviations Used

EW = end-of-weathering

GWB = Geochemist's Workbench

HAP = hydroxyapatite

I.S. = ionic strength

IUGS = International Union of Geological Sciences

PAL = present atmospheric level

 P_{CO2} = partial pressure of CO_2

T = temperature